Ultrasonics Sonochemistry 94 (2023) 106331

Contents lists available at ScienceDirect

Ultrasonics Sonochemistry

journal homepage: www.elsevier.com/locate/ultson

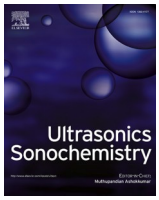

Piezoelectric atomization of liquids with dynamic viscosities up to 175 cP at room temperature

Tang Xie [1], Yaohua Zeng [1], Zhenzhen Gui, Mingdong Ma, Yuxuan Huo, Weirong Zhang, Tian Tan, Tao Zou [*], Fan Zhang [*], Jianhui Zhang [*]

School of Mechanical and Electrical Engineering, Guangzhou University, 230 Wai Huan Xi Road, Guangzhou Higher Education Mega Center, Guangzhou 510006, China

ARTICLE INFO

Keywords:
Piezoelectric atomization
High viscosity
Vibration coupling
Elliptic motion
Cavitation effect
Raman spectroscopy

ABSTRACT

Piezoelectric atomization has been applied in the field of respiratory medicine delivery and chemistry. However, the wider application of this technique is limited by the viscosity of the liquid. High-viscosity liquid atomization has great potential for applications in aerospace, medicine, solid-state batteries and engines, but the actual development of atomization is behind expectations. In this study, instead of the traditional model of single-dimensional vibration as a power supply, we propose a novel atomization mechanism that uses two coupled vibrations to induce micro-amplitude elliptical motion of the particles on the surface of the liquid carrier, which produces a similar effect as localized traveling waves to push the liquid forward and induce cavitation to achieve atomization. To achieve this, a flow tube internal cavitation atomizer (FTICA) consisting of a vibration source, a connecting block and a liquid carrier is designed. The prototype can atomize liquids with dynamic viscosities up to 175 cP at room temperature with a driving frequency of 507 kHz and a voltage of 85 V. The maximum atomization rate in the experiment is 56.35 mg/min, and the average atomized particle diameter is 10 μm. Vibration models for the three parts of the proposed FTICA are established, and the vibration characteristics and atomization mechanism of the prototype were verified using the vibration displacement measurement experiment and the spectroscopic experiment. This study offers new possibilities for transpulmonary inhalation therapy, engine fuel supply, solid-state battery processing and other areas where high-viscosity microparticle atomization is needed.

1. Introduction

Atomization is the process by which a continuous liquid is dispersed into a two-phase flow of small particle droplets. Ultrasonic atomization refers to an atomization process where an ultrasonic atomizer applies a driving frequency higher than 20 kHz. In general, the higher the driving frequency is, the smaller the atomized particles [1]. Most of ultrasonic atomizers operate in the piezoelectric driving mode, as this mode yields low energy consumption, high efficiency, simple structure, small atomized particles and low cost [2–5]. Therefore, ultrasonic atomizers are widely used in the aerospace and medical fields, engines, solid-state batteries, food, and environmental improvement and quality of life improvement applications [6–8].

The first study on ultrasonic atomization was carried out by Wood and Loomis [9]. Afterward, the ultrasonic atomization industry developed at a high speed. Currently, there are three main types of ultrasonic atomizers, namely, surface acoustic wave (SAW) atomizers [10–12], static mesh atomizers [13–15] and dynamic mesh atomizers [16–18], which are widely used for the conventional atomization of water, liquid fuels and detergents [16,19–22].

In recent years, various milestones have been reached due to the rapid development of research on ultrasonic atomization. Particularly in the fields of pharmaceutical inhalation therapy, fuel injection and solid-state batteries, ultrasonic atomizers have great potential for application. For upper respiratory tract and pulmonary diseases, inhalation therapy allows direct access to the affected area, significantly reduces medicine dosage required, and reduces side effects and adherence compared to those of traditional oral and intravenous medicine administration [23,24]. For fuel injection atomization, ultrasonic atomization not only consumes less energy than conventional pressure atomization but also yields smaller atomized particles, thereby allowing the fuel to burn more fully and reducing the harm to the environment from combustion

* Corresponding authors.
E-mail addresses: tzou@gzhu.edu.cn (T. Zou), zhf_jd@gzhu.edu.cn (F. Zhang), zhangjh@nuaa.edu.cn (J. Zhang).
[1] Tang Xie, Yaohua Zeng are co-first authors of this article.

https://doi.org/10.1016/j.ultsonch.2023.106331
Received 18 December 2022; Received in revised form 10 February 2023; Accepted 11 February 2023
Available online 13 February 2023

products. For solid-state batteries, binders are used to bond the electrode material to the current collector and are usually present in less than 10% of electrodes [25]. The current commonly used process is mixing the binder with various electrode materials, enabling the electrode materials to be bonded together [26,27]. A few processes use pressure to atomize the binder and to spray it onto the electrode material. Compared to the method of mixing the binder and the electrode material, this atomization combination method yields smaller liquid binder particles, which allows a more uniform combination of the two, ultimately increasing the conductivity of the electrodes and improving the performance of the battery.

All three of the atomizer structures are used in the field of inhalation therapy. However, the viscosity of the liquid must be less than 7 cP [28], significantly limiting the variety of inhaled medicines and hindering the development of inhalation therapy with high-viscosity medicines, including herbs. Therefore, the study of high-viscosity liquid atomization for medical inhalation therapy has important significance and broad development prospects.

The viscosity of the fuel used in an engine is generally approximately 4 cP [29,30], and the current approach is to use ultrahigh pressure, up to 1500 bar, for atomization of high-viscosity liquids [31,32]. However, achieving high injection pressures requires very large amounts of energy, which is contrary to the original reason for atomizing fuel, reducing particle size and increasing combustion efficiency. Therefore, studying the atomization of high-viscosity liquids is important for improving engine combustion efficiency, reducing energy consumption and reducing carbon emissions.

The pressure atomization method used in solid-state batteries allows the bonding of the binder with the active material. Although this method of bonding allows more uniform bonding, the binder has a very high viscosity, of several thousand or even tens of thousands of centipoises [33], so pressure atomization requires very high energy consumption, and the atomization particle size is not sufficiently small, which affects the bonding uniformity. Therefore, the study of the atomization of high-viscosity liquids by ultrasonic atomization will provide important alternative ideas in the field of solid-state batteries processing.

Researchers have explored the piezoelectric atomization of highly viscous liquids. In 2010, A. Lozano et al. used a piezoelectric ceramic disc structure to achieve ultrasonic atomization of liquids with a kinematic viscosity of 28 cSt [34]. In 2017, Junhui Law et al. implanted a microheater into an atomization device to achieve atomization of liquids with viscosities of 1 cP – 200 cP, using heating to generate large amounts of gas nuclei [35]. However, heat could destroy or degrade medicines, and the design is too complex to be used in the pharmaceutical field. In 2021, Axel Lefebure et al. designed an apparatus with a fibrous liquid delivery column at the lower end of a grid atomizer to atomize a high-viscosity biodegradable oil with a kinematic viscosity of 37 cSt (dynamic viscosity of approximately 30 cP), representing the highest viscosity liquid atomized at room temperature to date [36].

With the current ultrasonic atomizers, when liquid viscosity increases from 1 cP to 100 cP, the unit atomization energy increases tens or even hundreds of times, posing an extreme challenge of the traditional atomization mechanism and structure. This study does not employ the idea of increasing energy density in the traditional structure to achieve atomization of high-viscosity liquids but rather overcomes the limitation of using one single-dimensional vibration as the atomization actuation power source in the traditional structure. Based on the above principle, we propose a novel FTICA with two dimensions of vibration synthesis for actuation and use cavitation caused by vibration to achieve liquid atomization.

The novel FTICA proposed in this study was inspired by the ultrasonic motor principle [37]. An ultrasonic motor uses two vibrations of the same frequency and different phases perpendicular to each other, so the surface particles of the stator of the ultrasonic motor form an elliptical trajectory, thus driving an object to move by friction [38]. Due to its simple structure, small size, light weight, fast response time, low noise level, large torque at low speed, good control characteristics, self-locking characteristic under power failure, freedom from magnetic field interference, and accurate motion [39,40], ultrasonic motors are widely used in the automotive, aerospace, precision manufacturing, optical scanning, biotechnology and medicine [41–47], and energy harvesting fields [48–51].

By working principle, ultrasonic motors can be divided into three main categories [52,53]: traveling wave type [54,55], standing wave type [56,57] and composite type [58,59]. However, all these studies address the movement of only solids and are rarely used in the field of liquid atomization.

In this study, the use of coupled longitudinal vibration and bending vibration as the actuation force is proposed as an alternative to the use of traditional one-dimensional vibration, and this idea is combined with cavitation theory to design a novel FTICA structure that can atomize liquids with viscosities up to 175 cP at room temperature. The proposed design uses a single piezoelectric driving source to generate longitudinal vibration and bending vibration at the same time. The two couple to form micro-amplitude elliptical motion, on the one hand, to drive the liquid forward, and on the other hand, to cavitate the liquid to achieve atomization. In this study, the vibration model of each part was established for the proposed coupled FTICA structure, and a set of theoretical solutions were obtained at a frequency of 507 kHz. A prototype was designed and built, and atomization experiments were conducted using liquids with viscosities of 50–175 cP to verify the feasibility of the FTICA design. The vibration displacements of each component of the FTICA were measured using a three-dimensional Doppler vibrometer to verify the correctness of the theoretical model. Full-spectrum experiments and Raman spectroscopy experiments were designed to verify the feasibility of the cavitation theory. This study provides a new atomization mechanism and atomization structure to address the problem of the ultrasonic atomization of high-viscosity liquids, providing a new direction for inhalation therapy, engine fuel atomization, solid-state batteries, aromatic essential oils and other applications that depend on high-viscosity liquids.

2. Material and methods

2.1. The structure of FTICA

Fig. 1 shows the structure of the FTICA in this study, which was composed of a vibration source, a connecting block and a liquid carrier, and the vibration source consists of a piezoelectric ceramic and a metal base. The piezoelectric ceramic was made of PZT, and the other structures were made of 304 stainless steel. The piezoelectric ceramic was under the vibration source, and the upper and lower ends of the connecting block were connected to the vibration source and the liquid carrier by welding. The main parameters of the FTICA are shown in Fig. 1(b) and Table 1, and a photograph of the prototype is shown in Fig. 1(c).

2.2. Ratio of liquid viscosity and analysis of impedance

In this experiment, propylene glycol liquid (with a dynamic viscosity of approximately 50 cP at room temperature) and vegetable glycerin liquid (with a dynamic viscosity of approximately 700 cP at room temperature) were used as the base liquids and were mixed according to the ratios shown in Table 2. The actual viscosities were measured using a rotary viscometer (NDJ-1, LICHEN, Shanghai, China) and are shown in Fig. 2(a).

To initially determine the resonance points for subsequent atomization experiments, an impedance analyzer (LCR Meter 6630, MICROTEST, Taiwan, China) was used to analyze the impedance of the whole FTICA. The experimental setup is shown in Fig. 2(b).

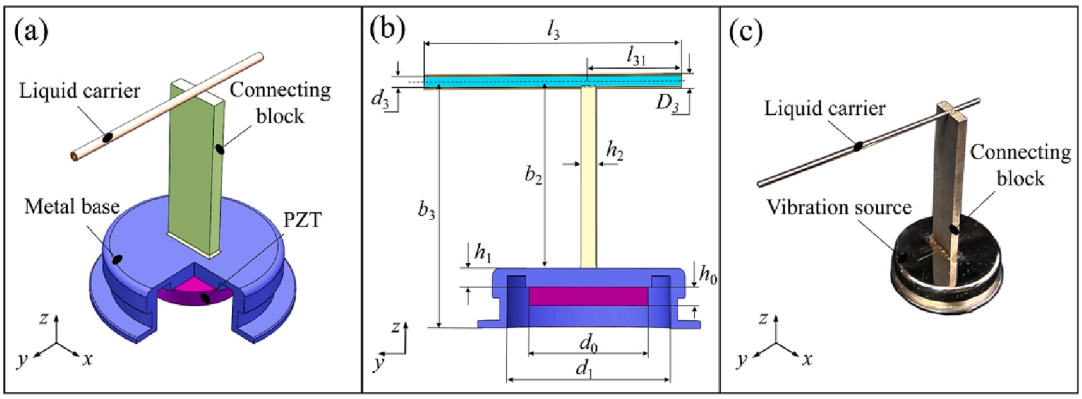

Fig. 1. Structure of the FTICA: (a) Three-dimensional structure; (b) Two-dimensional cross-section; (c) Photograph of the prototype.

Table 1
Main dimensional values of the FTICA.

Parameters	Values
Diameter/d_0 (mm)	18.00
Thickness/h_0 (mm)	1.00
Diameter/d_1 (mm)	24.00
Thickness/h_1 (mm)	4.00
Height/b_2 (mm)	36.00
Thickness/h_2 (mm)	1.00
Height/b_3 (mm)	46.00
Diameter/D_3 (mm)	1.00
Diameter/d_3 (mm)	0.80
Distance/l_3 (mm)	45.00
Distance/l_{31} (mm)	10.00

Table 2
Mixing ratio of liquid for atomization.

Propylene Glycol share	Vegetable Glycerin share	Actual measured viscosity (cP)
100%	0%	50
88.2%	11.8%	75
76.1%	23.9%	100
69.2%	30.8%	125
62.3%	37.7%	150
56.5%	43.5%	175

2.3. Measurement of atomization rate and atomized particle sizes

To verify the atomization effect of the FTICA proposed in this study, measurements of the atomization rate were carried out; the experimental system is shown in Fig. 3(a). The atomization rate was obtained using a precision analytical balance (FA2204, LICHEN, Shanghai, China) to measure the mass of the liquid reservoir bottle before and after atomization and a peristaltic pump to deliver of the liquid.

The atomized particle diameters and their distributions were measured using a spray laser particle size analyzer (Winner311XP, Winner Particle, Jinan, China); the experimental setup is shown in Fig. 3 (b).

2.4. Experiments of vibration measurement

Vibration displacement measurements of the three-part structure of the FTICA were carried out using two types of laser Doppler measuring vibration instruments. Due to the large vibration area of the vibration source and the Connecting Body, a three-dimensional scanning laser (LV-SC400, SOPTOP, Zhejiang, China) was used to measure the displacements. Fig. 4(a) - Fig. 4(b) shows the displacement measurement setup.

Due to the small diameter of the liquid carrier, a single-point laser vibrometer (LV-S01, SOPTOP, Zhejiang, China) was selected, coordinating with a precision displacement stage. The displacement of the bending vibration in the liquid carrier diameter direction and longitudinal vibration in the axis direction were measured; the experimental

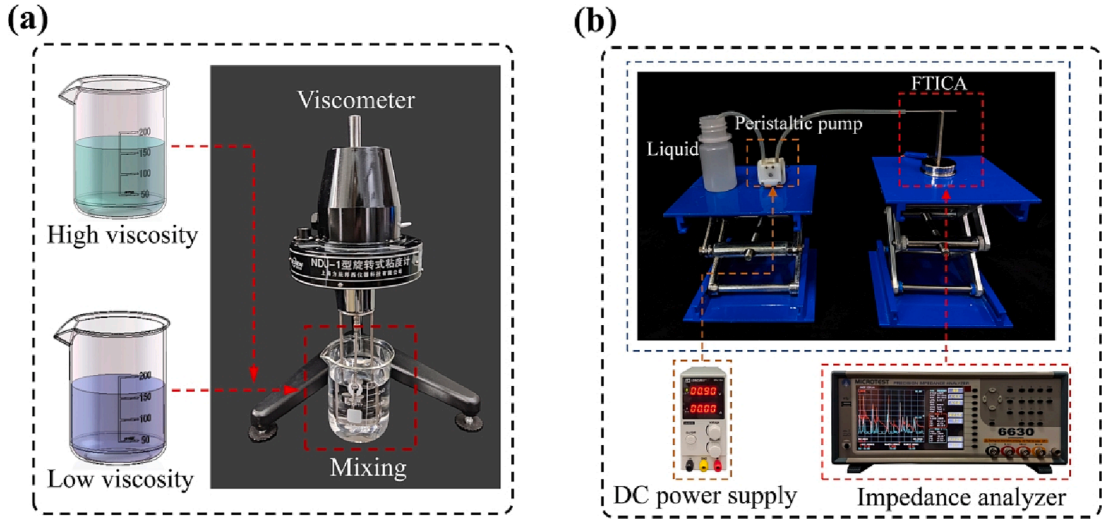

Fig. 2. Preliminary experiment: (a) Configuration diagram for different viscosity liquids; (b) Diagram of the experimental setup for impedance analysis.

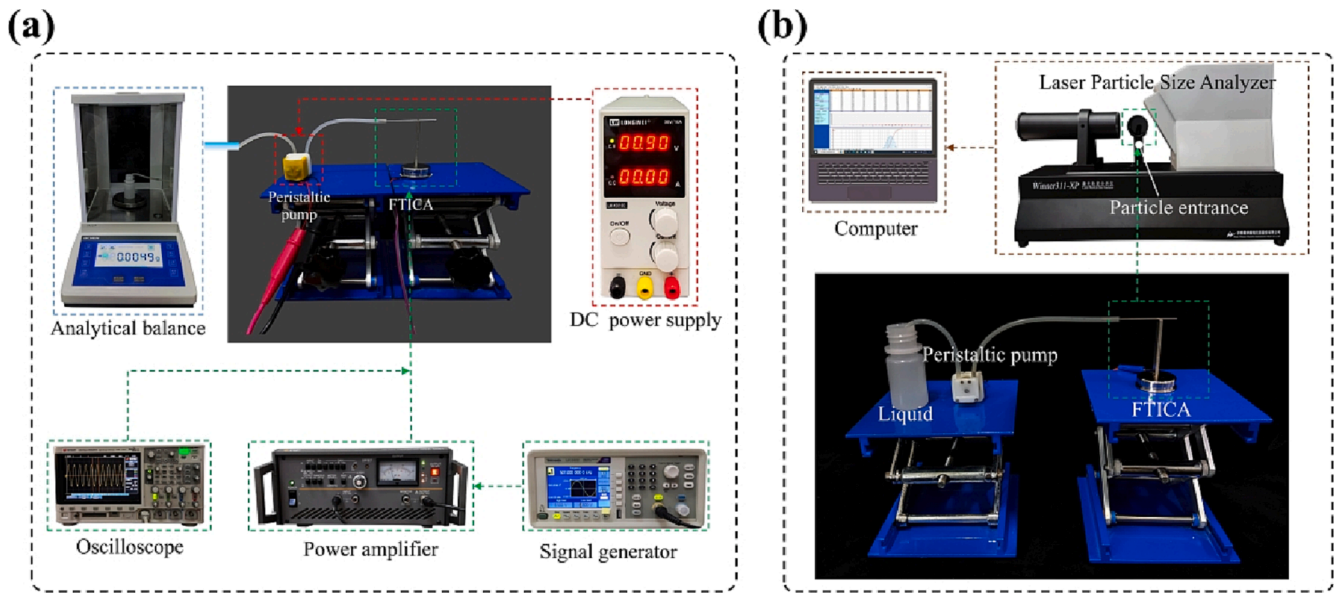

Fig. 3. Diagram of atomization experimental setup: (a) Diagram of atomization rate experimental setup; (b) Diagram of the experimental setup for particle size testing.

setup is shown in Fig. 4(c).

2.5. Experiments of spectral measurement

Raman spectroscopy was used to verify whether the molecular structure of the liquid changes from before to after atomization. The experimental setup for the microscopic Raman spectroscopy (ATR8300, OPTOSKY, Fujian, China) is shown in Fig. 5(a).

A high-power light source transmitter and receiver (ATG1100, OPTOSKY, Fujian, China) was used to analyze the absorbance and light intensity of the liquid before and after atomization. The experimental setup for the absorption spectroscopy measurements is shown in Fig. 5 (b).

3. Theory and calculation

3.1. Theory of liquid movement

According to the theory of dynamics, if a particle vibrates with the same frequency and different phases in two mutually perpendicular directions, the trajectory of the particle is an ellipse. Currently, this motion is known as elliptical motion. For the liquid carrier, if all the particles on the tube wall undergo micro-amplitude elliptical motion, the liquid inside the liquid carrier moves due to contact with the moving particles. Therefore, the analysis of liquid movement theory translates into the analysis of the micro-amplitude elliptical motion of a particle on the tube wall.

We designed a vibration source consisting of a piezoelectric ceramic and a metal base, and we used an eccentrically mounted connecting block to achieve orthogonal vibrations of the same frequency and different phases and to ultimately achieve propulsion and atomization of the liquid in the liquid carrier. Carrying out a vibration transfer analysis of the whole FTICA would be very complex and impractical, so we split the whole FTICA into three parts for vibration transfer analysis according to the different parts of the structure: vibration source vibration analysis, connecting block vibration analysis and liquid carrier vibration analysis.

For clear and unambiguous vibration analysis of the three parts, it is necessary to establish separate coordinate systems for each part. Fig. 6 shows the establishment of the coordinate systems for each part. To keep the established coordinates clear, we use subscripts to represent the parameters in the coordinate system. X_{ij} denotes the X coordinate of the j-th variable in the i-th structure, where$i = 1, 2, 3$. For example, we refer to X_{30} in section 3.1.3 of the paper meaning a variable in the third structure (liquid carrier). The structure of the FTICA is shown in Fig. 6 (a). The simplified circular thin plate coordinate system of the vibration source is set to$o_1 - r_1 - \theta_1 - z_1$, and the eccentricity of the circular thin plate coordinate origin and the connecting block coordinate origin ise_{12}, as shown in Fig. 6(b). The connecting block coordinate system is set as$o_2 - x_2 - y_2 - z_2$, as shown in Fig. 6(c). We set the liquid carrier coordinate system as $o_3 - x_3 - y_3 - z_3$ and the eccentricity between the connecting block coordinate origin and the liquid carrier coordinate origin ase_{23}, as shown in Fig. 6(d). Moreover, the magnitude and direction of the force in the forced vibration are indicated for each part in the upper right corners of Fig. 6(b), Fig. 6(c) and Fig. 6(d), respectively. Note that the component forces along the y_2 direction are not represented for the connecting block, as only bending vibrations are considered and not vibrations along the y_2 direction.

3.1.1. Vibration analysis of the vibration source

The vibration source model can be simplified to a circular thin plate with fixed supports all around, where the radius isa_1, the thickness ish_1, the material density isρ_1, the modulus of elasticity is E_1 and the Poisson ratio isμ_1, as shown in Fig. 6(b). Using the relationship between the polar coordinates r_1 andθ_1, and the Cartesian coordinates x_1 andz_1, the partial differential equation for the displacement of a circular thin plate can be expressed as [60–63]:

$$\frac{\partial^2 w_1}{\partial t_1^2} + \left(\frac{D_1}{\rho_1 h_1}\right)^2 \left(\frac{\partial^2}{\partial r_1^2} + \frac{1}{r_1}\frac{\partial}{\partial r_1^2} + \frac{1}{r_1^2}\frac{\partial^2}{\partial \theta_1^2}\right)^2 w_1 = 0 \tag{1}$$

where $D_1 = \frac{E_1 h_1^3}{12(1-\mu_1^2)}$ is the bending stiffness of the plate, and w_1 is the vibrational displacement.

Due to the symmetry of the circular thin plate, the above equation can be solved as [63]:

$$w_1(r_1, \theta_1, t_1) = R(r_1)(S_{n1}\sin n_1\theta_1 + E_{n1}\cos n_1\theta_1)e^{i\omega_a t_1} \tag{2}$$

where ω_a is the natural frequency of the circular thin plate, $R(r_1)S_{n1}\sin n_1\theta_1$ and $R(r_1)E_{n1}\sin n_1\theta_1$ are the basis functions that form the function space.

For a circular thin plate with fixed perimeter support, the boundary

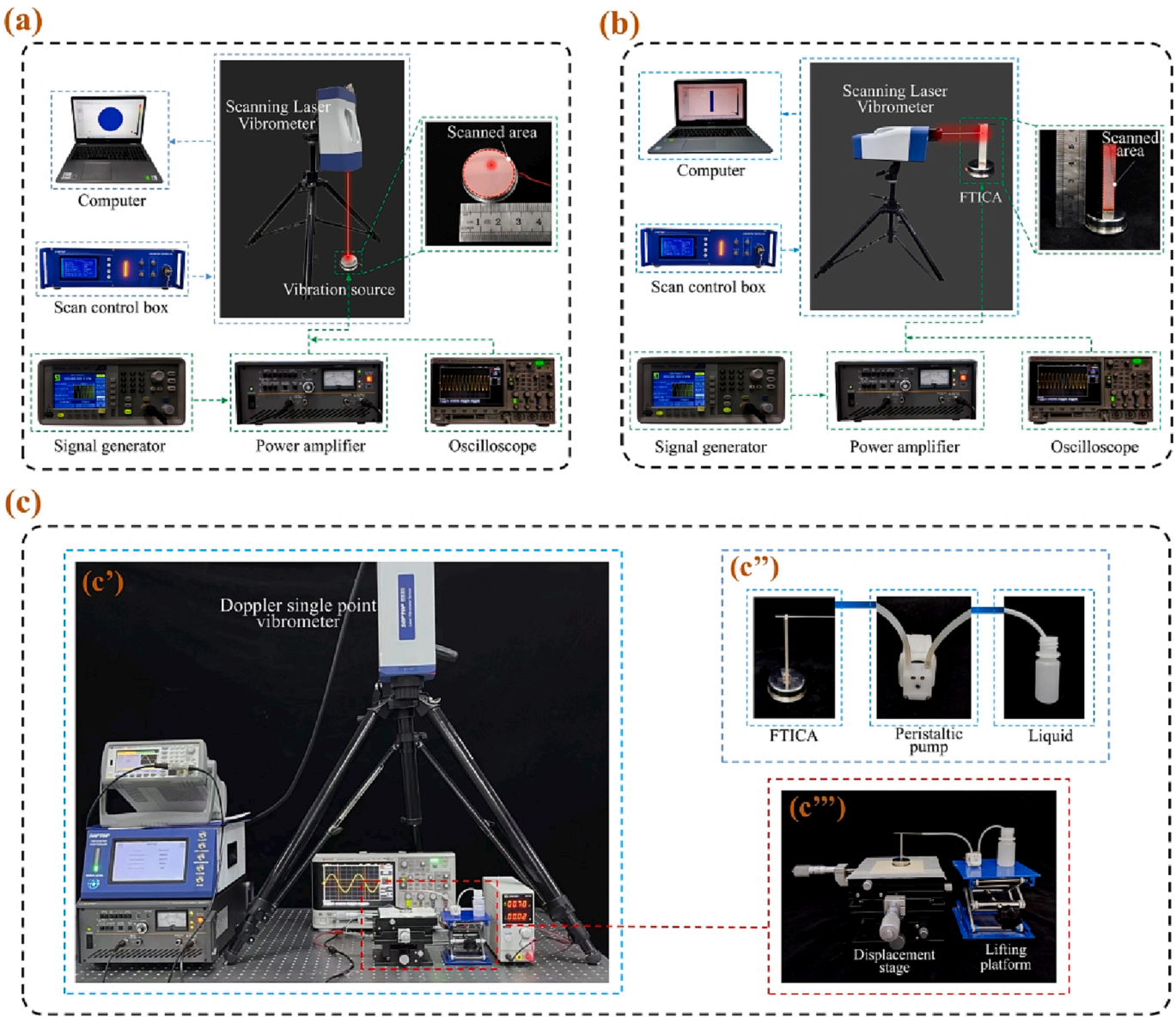

Fig. 4. Diagram of the displacement measurement setup: (a) Diagram of the vibration experimental setup for the vibration source; (b) Diagram of the vibration experimental setup for the Connecting Body; (c) Diagram of the vibration experimental setup for the liquid carrier; (c') Overall experimental setup; (c'') FTICA fluid supply system; (c''') Displacement stage partial enlargement.

conditions can be expressed as [60]:

$$R(a_1) = 0, R^{'}(a_1) = 0 \tag{3}$$

Using boundary conditions, the natural frequency of the circular thin plate can be found, which is expressed as:

$$\omega_a = \omega_{m1n1} = \frac{\lambda_{m1n1}}{a_1^2}\sqrt{\frac{D_1}{\rho_1 h_1}} \tag{4}$$

where m_1 denotes the number of nodal circles; n_1 indicates the number of nodal diameters; and λ_{m1n1} indicates the natural frequency constant.

Thereby, the mode function of the circular thin plate can be obtained, which is expressed as:

$$\Phi_{m1n1}(r_1,\theta_1) = \mathrm{A}_{n1}\left\{J_{n1}(k_1 r_1) - \frac{J_{n1}(\lambda_{m1n1})}{I_{n1}(\lambda_{m1n1})} I_{n1}(k_1 r_1)\right\}(\mathrm{S}_{n1}\sin n_1\theta_1 + \mathrm{E}_{n1}\cos n_1\theta_1) \tag{5}$$

where $k_1^4 = \frac{\omega_a^2 \rho_1 h_1}{D_1}$.

At this point, the forced vibration of the circular thin plate can be analyzed in terms of the mode function and the natural frequency. As shown in Fig. 6(b), the distributed excitation force of the piezoelectric ceramic acting on a uniform thin plate with frequency ω_0 is $f_a(r_1,\theta_1,t_1) = F_a(r_1,\theta_1)\mathrm{e}^{i\omega_0 t_1}$. This distributed excitation force can be derived from the piezoelectric equation [60].

The following is a method for determining the forced vibration response of the circular thin plate using distributed excitation force. The displacement response of a thin plate to forced vibration with small deflection is expressed using the normalized displacement modes of each order of the plate as [60–62]:

$$w_2(r_1,\theta_1,t_1) = \sum_{m_1=0}^{\infty}\sum_{n_1=0}^{\infty}\Phi_{m_1n_1}(r_1,\theta_1)q_{m_1n_1}(t_1) \tag{6}$$

where $\Phi_{m_1n_1}(r_1,\theta_1)$ is the normalized displacement mode of each order of the thin plate and satisfies the orthogonality condition for the thin plate vibration mode. $q_{m_1n_1}(t_2)$ corresponds to the generalized coordinates of $\Phi_{m_1n_1}(r_1,\theta_1)$.

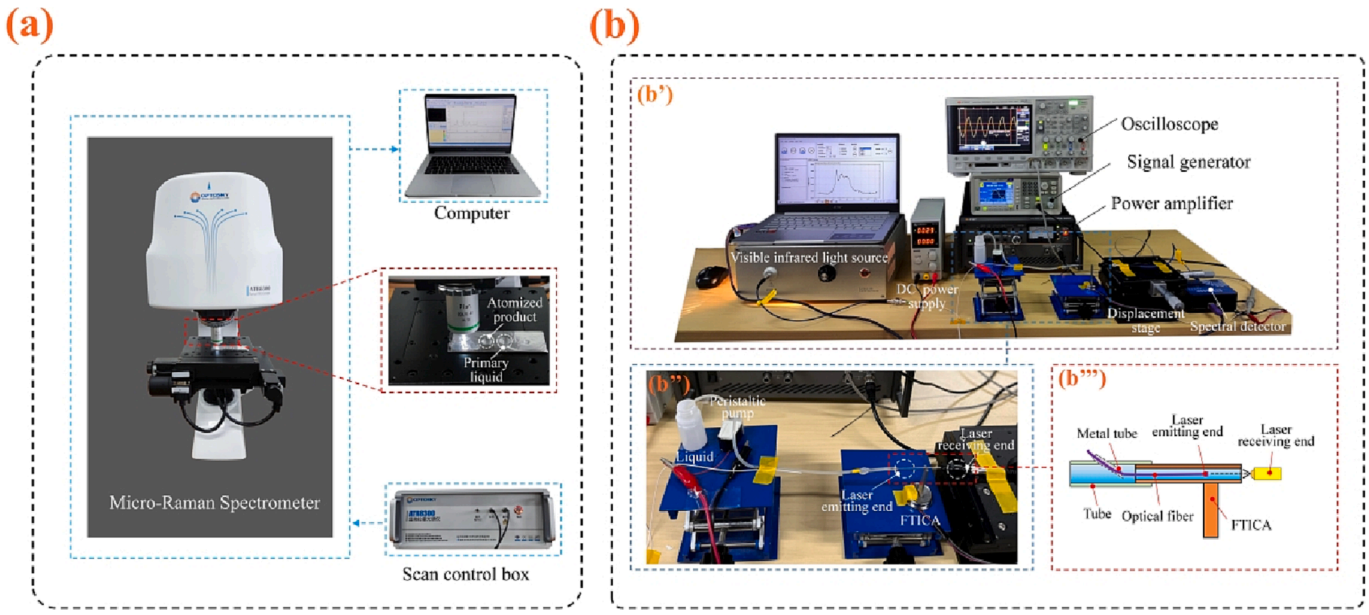

Fig. 5. Diagram of spectroscopy experimental setup: (a) Diagram of the experimental setup for micro-Raman spectroscopy; (b)Diagram of the spectral absorbance experimental setup; (b') Overall experimental setup; (b'') Enlarged view of the optical fiber connection; (b''') Schematic diagram of the optical fiber connection.

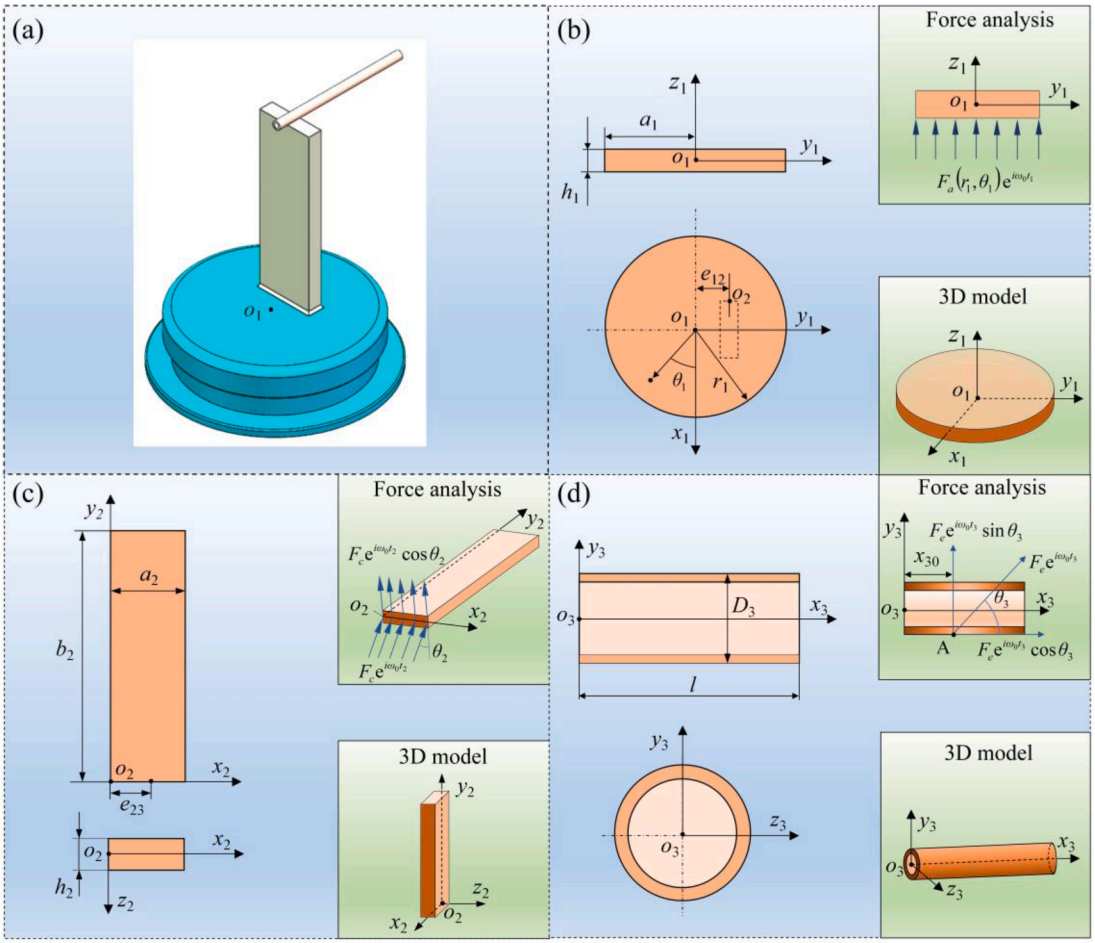

Fig. 6. Coordinate systems for each part: (a) Overall atomizer; (b) Vibration source coordinate system; (c) Connecting block coordinate system; (d) Liquid carrier coordinate system.

Using excitation force, we can obtain the displacement deflection forcing response of a uniformly thin plate:

$$w_2(r_1,\theta_1,t_1)=\sum_{m_1=0}^{\infty}\sum_{n_1=0}^{\infty}\frac{F_{m_1n_1}\Phi_{m_1n_1}(r_1,\theta_1)e^{i\left(\omega_0 t_1-\varphi_{m_1n_1}\right)}}{\left[K_{m_1n_1}\sqrt{\left(1-\overline{\omega}_{m_1n_1}^2\right)^2+\left(2\xi_{m_1n_1}\overline{\omega}_{m_1n_1}\right)^2}\right]} \tag{7}$$

where $\overline{\omega}_{m_1n_1}=\frac{\omega_0}{\omega_{m_1n_1}}$ is the ratio of the excitation frequency to the natural frequency of the system vibration, $\xi_{m_1n_1}=\frac{C}{2M_{m_1n_1}\omega_{m_1n_1}}$ is the relative damping factor of the system, C is the damping, and $\varphi_{m_1n_1}=\tan^{-1}\left(\frac{2\xi_{m_1n_1}\overline{\omega}_{m_1n_1}}{1-\overline{\omega}_{m_1n_1}^2}\right)$ is the phase of the system.

When$\omega_0=\omega_{m_1n_1}$, the circular thin plate is in resonance of orderm_1n_1, and the displacement deflection forcing response is mainly of orderm_1n_1. Therefore, the displacement deflection forcing response can be expressed as:

$$w_2(r_1,\theta_1,t_1)=\frac{F_{m_1n_1}\Phi_{m_1n_1}(r_1,\theta_1)e^{i\left(\omega_0 t_1-\varphi_{m_1n_1}\right)}}{\left[K_{m_1n_1}\sqrt{\left(1-\overline{\omega}_{m_1n_1}^2\right)^2+\left(2\xi_{m_1n_1}\overline{\omega}_{m_1n_1}\right)^2}\right]} \tag{8}$$

After finding the forced response of displacement deflection at resonance, we use the displacement deflection forcing response function $w_2(r_1,\theta_1,t_1)$ to find the second order partial derivative for timet_1. Thereby, the acceleration of the vibration source at any point in the vibration mode can be obtained:

$$\frac{\partial^2 w_2(r_1,\theta_1,t_1)}{\partial t_1^2}=-\omega_0^2\frac{F_{m_1n_1}\Phi_{m_1n_1}(r_1,\theta_1)e^{i\left(\omega_0 t_1-\varphi_{m_1n_1}\right)}}{\left[K_{m_1n_1}\sqrt{\left(1-\overline{\omega}_{m_1n_1}^2\right)^2+\left(2\xi_{m_1n_1}\overline{\omega}_{m_1n_1}\right)^2}\right]} \tag{9}$$

After finding the acceleration from Eq. (9), assuming that the mass of the point ism_0, then we can express the force as:

$$f_b(r_1,\theta_1,t_1)=-m_0\omega_0^2\frac{F_{m_1n_1}\Phi_{m_1n_1}(r_1,\theta_1)e^{i\left(\omega_0 t_1-\varphi_{m_1n_1}\right)}}{\left[K_{m_1n_1}\sqrt{\left(1-\overline{\omega}_{m_1n_1}^2\right)^2+\left(2\xi_{m_1n_1}\overline{\omega}_{m_1n_1}\right)^2}\right]} \tag{10}$$

3.1.2. Vibration analysis of the connecting block

The deflection of a connecting block under free bending vibration can be expressed as a characteristic orthogonal polynomial in the $\times$ and y directions [64,65], expressed as:

$$W(x,y)=\sum_{m_2}\sum_{n_2}A_{m_2n_2}\Phi_{m_2}(x)\Psi_{n_2}(y)m_2,n_2=1,2,3,\cdots,\infty \tag{11}$$

where x and y are dimensionless coordinates,$x=x_2/a_2$,$y=y_2/b_2$, x_2 and y_2 are the coordinates of the sides of the connecting block, $\Phi_{m_2}(x)$ and $\Psi_{n_2}(y)$ are the bending deflection of the connection block in the x and y directions, the length isa_2, the width isb_2, the thickness ish_2, the material density isρ_2, the modulus of elasticity is E_2 and the Poisson ratio isμ_2, as shown in Fig. 6(c).

The characteristic polynomial is solved by using the trial function to solve the first polynomial; then, a set of polynomials for a certain interval is generated using the Gram-Schmidt process [64].

By substituting the deflection function into the kinetic and strain energy expressions and minimizing the Rayleigh quotient with respect to the coefficient A [61], we can express the resulting characteristic equation as [64]:

$$\sum_{m_2}\sum_{n_2}\left[C_{m_2n_2i_2j_2}-\lambda_b E_{m_2i_2}^{(0,0)}F_{n_2j_2}^{(0,0)}\right]A_{m_2n_2}=0 \tag{12}$$

$$C_{m_2n_2i_2j_2}=E_{m_2i_2}^{(2,2)}F_{n_2j_2}^{(0,0)}+\alpha^4E_{m_2i_2}^{(0,0)}F_{n_2j_2}^{(2,2)}+\mu_2\alpha^2\left[E_{m_2i_2}^{(0,2)}F_{n_2j_2}^{(2,0)}+E_{m_2i_2}^{(2,0)}F_{n_2j_2}^{(0,2)}\right]+2(1-\mu_2)\alpha^2E_{m_2i_2}^{(1,1)}F_{n_2j_2}^{(1,1)} \tag{13}$$

$$E_{m_2i_2}^{(r_2,s_2)}=\int_0^1\left(\frac{d^{r_2}\Phi_m}{dx^{r_2}}\right)\left(\frac{d^{s_2}\Phi_i}{dx^{s_2}}\right)dx,F_{n_2j_2}^{(r_2,s_2)}=\int_0^1\left(\frac{d^{r_2}\psi_n}{dy^{r_2}}\right)\left(\frac{d^{s_2}\psi_j}{dy^{s_2}}\right)dy \tag{14}$$

where $\alpha=\frac{a_2}{b_2}$ is the side ratio;$m_2,n_2,i_2,j_2=1,2,3,\cdots,\infty$; $\lambda_b=\frac{\rho_2h_2\omega_b^2a_2^4}{D_2}$ is the natural frequency parameter; $D_2=\frac{E_2h_2^3}{12\left(1-\mu_2^2\right)}$ is the bending stiffness of the connecting block; $r_2,s_2=0,1,2$ is the order of derivation.

The solution of the characteristic equation produces the natural frequency and vibration mode of the connecting block, and the characteristics of the bending vibrations of the connecting block can be analyzed with these parameters.

As shown in Fig. 6(c), an exciting force $f_c=F_ce^{i\omega_0t_2}\cos\theta_2$ acts at point (x_0,y_0) of the connecting block, where angle θ_2 is the angle between the excitation force f_c and the steady-state response force f_b in the upper phase. The size of this angle is determined by the eccentricity e_{12} of the connecting block coordinate origin to the circular plate coordinate origin and the forced response of the circular plate vibration displacement. Since the excitation force is provided by the steady-state response of the upper stage force, it is assumed that point (x_0,y_0) on the connecting block corresponds to point (r_{10},θ_{10}) on the circular thin plate, and the expression for the excitation force f_c can be rewritten as:

$$f_c=F_ce^{i\left(\omega_0t_1-\varphi_{m_1n_1}\right)}\cos\theta_2 \tag{15}$$

where ω_0 is the excitation frequency, the same as in the previous stage, and F_c is the amplitude of the excitation force.

Thus, the steady-state response of forced vibrations can be derived and expressed as:

$$w_3(x,y,t_1)=\sum_{m_2=0}^{\infty}\sum_{n_2=0}^{\infty}\frac{F_cW_{m_2n_2}(x_0,y_0)W_{m_2n_2}(x,y)e^{i\left(\omega_0t_1-\varphi_{m_1n_1}-\varphi_{m_2n_2}\right)}\cos\theta_2}{\left[M_{m_2n_2}\omega_{m_2n_2}^2\sqrt{\left(1-\overline{\omega}_{m_2n_2}^2\right)^2+\left(2\xi_{m_2n_2}\overline{\omega}_{m_2n_2}\right)^2}\right]} \tag{16}$$

where $W_{m_2n_2}(x,y)$ is a mode function of the connecting block; $M_{m_2n_2}$ is the modal quality; $\xi_{m_2n_2}$ is the relative damping factor; $\overline{\omega}_{m_2n_2}=\frac{\omega_0}{\omega_{m_2n_2}}$ is the ratio of the excitation frequency to the natural frequency of the system vibration; $\varphi_{m_2n_2}=\tan^{-1}\left(\frac{2\xi_{m_2n_2}\overline{\omega}_{m_2n_2}}{1-\overline{\omega}_{m_2n_2}^2}\right)$ is the system vibration phase.

When$\omega_0=\omega_{m_2n_2}$, the connecting block is in resonance, and the displacement deflection forcing response is dominated by the m_2n_2 mode. Therefore, the displacement deflection forcing response is expressed as:

$$w_3(x,y,t_1)=\frac{F_cW_{m_2n_2}(x_0,y_0)W_{m_2n_2}(x,y)e^{i\left(\omega_0t_1-\varphi_{m_1n_1}-\varphi_{m_2n_2}\right)}\cos\theta_2}{\left[M_{m_2n_2}\omega_{m_2n_2}^2\sqrt{\left(1-\overline{\omega}_{m_2n_2}^2\right)^2+\left(2\xi_{m_2n_2}\overline{\omega}_{m_2n_2}\right)^2}\right]} \tag{17}$$

After finding the forced response of the displacement deflection at resonance, we obtain the second order partial derivative for time t_1 using the displacement deflection forcing response function$w_3(x,y,t_1)$. The acceleration of the connecting block at any point under the $B_{m_2n_2}$ vibration mode can be obtained:

$$\frac{\partial^2 w_3(x,y,t_1)}{\partial t_2^2}=-\omega_0^2\frac{F_cW_{m_2n_2}(x_0,y_0)W_{m_2n_2}(x,y)e^{i\left(\omega_0t_1-\varphi_{m_1n_1}-\varphi_{m_2n_2}\right)}\cos\theta_2}{\left[M_{m_2n_2}\omega_{m_2n_2}^2\sqrt{\left(1-\overline{\omega}_{m_2n_2}^2\right)^2+\left(2\xi_{m_2n_2}\overline{\omega}_{m_2n_2}\right)^2}\right]} \tag{18}$$

After finding the acceleration from Eq. (18), assuming the mass of the

point ism_1, we can express the force on the point as:

$$f_d(x,y,t_1) = -\omega_0^2 m_1 \frac{F_c W_{m_2n_2}(x_0,y_0) W_{m_2n_2}(x,y) e^{i\left(\omega_0 t_1 - \varphi_{m_1n_1} - \varphi_{m_2n_2}\right)} \cos\theta_2}{\left[M_{m_2n_2}\omega_{m_2n_2}^2 \sqrt{\left(1-\overline{\omega}_{m_2n_2}^2\right)^2 + \left(2\xi_{m_2n_2}\overline{\omega}_{m_2n_2}\right)^2}\right]} \quad (19)$$

3.1.3. Vibration analysis of the liquid carrier

For the liquid carrier, the model is a cylindrical shell of a finite length. Shell vibration is complex, with displacements in all three directions at the same time, and there is no universally accepted, unified theory for shell vibration [60]. To study the micro-amplitude elliptical motion of particles on the inner surface of the liquid carrier, only two mutually perpendicular vibrations at the same frequency with different phases are considered, the bending vibration and longitudinal vibration of the shell. The surface motion of the shell is ignored, so the cylindrical shell model is simplified to a beam.

In Fig. 6(d), the total length of the liquid carrier isl_3, the outer diameter isD_3, the material density isρ_3, the modulus of elasticity is E_3 and the Poisson ratio isμ_3. According to the force analysis in Fig. 6(d), the steady-state response of the longitudinal vibration of a liquid carrier with free boundary conditions at both ends needs to be solved.

First, we assume that $f_e = F_e e^{i\omega_0 t_3}\cos\theta_3$ is the longitudinal excitation force at this stage and that the liquid carrier contact point (x_{30}, y_{30}) corresponds to point (x_0, y_0) on the connecting block. Then, the longitudinal excitation force f_e can be rewritten as:

$$f_e = F_e e^{i\left(\omega_0 t_1 - \varphi_{m_1n_1} - \varphi_{m_2n_2}\right)}\cos\theta_3 \quad (20)$$

where $\varphi_{m_1n_1} + \varphi_{m_2n_2} = \varphi_0$.

It is possible to obtain:

$$f_e = F_e e^{i(\omega_0 t_1 - \varphi_0)}\cos\theta_3 \quad (21)$$

where ω_0 is the excitation frequency, the same as in the previous stage, and F_e is the amplitude of the excitation force.

The displacement steady-state response to the longitudinal vibration of a liquid carrier can be expressed according to the principle of the superposition of the vibration mode as:

$$u_1(x_3,t_1) = \sum_{n_3=1}^{\infty} W_{n_3}(x_3) q_{n_3}(t_1) = \sum_{n_3=1}^{\infty} \frac{F_e\cos\theta_3 e^{i\left(\omega_0 t_1 - \varphi_0 - \varphi_{n_3}\right)} W_{n_3}(x_{30}) W_{n_3}(x_3)}{\left[K_{n_3}\sqrt{\left(1-\overline{\omega}_{n_3}^2\right) + \left(2\xi_{n_3}\overline{\omega}_{n_3}\right)^2}\right]} \quad (22)$$

where $W_{n_3}(x_3)$ is a function of the longitudinal vibration mode;$\varphi_{n_3} = \tan^{-1}\left(\frac{2\xi_{n_3}\overline{\omega}_{n_3}}{1-\overline{\omega}_{n_3}^2}\right)$; ω_{n_3} is the natural frequency of the longitudinal vibration; $\overline{\omega}_{n_3} = \frac{\omega_0}{\omega_{n_3}}$ is the ratio of the excitation frequency to the natural frequency of the longitudinal vibration of the system; ξ_{n_3} is the relative damping factor of the system; $K_{n_3} = \omega_{n_3}^2 \int_0^{l_3} \rho_3 S_3 W_{n_3}^2(x_3)\mathrm{d}(x_3)$ is the modal stiffness of the system; S_3 is the cross-sectional area of the beam corresponding to the outer diameter of the liquid carrier.

When$\omega_{n_3} = \omega_0$, the longitudinal vibration of the liquid carrier is resonant in ordern_3, and the displacement steady-state response is dominated by the vibration mode of ordern_3. Therefore, the displacement steady-state response can be simplified as:

$$u_1(x_3,t_1) = W_{n_3}(x_3) q_{n_3}(t_1) = \frac{F_e\cos\theta_3 e^{i\left(\omega_0 t_1 - \varphi_0 - \varphi_{n_3}\right)} W_{n_3}(x_{30}) W_{n_3}(x_3)}{\left[K_{n_3}\sqrt{\left(1-\overline{\omega}_{n_3}^2\right) + \left(2\xi_{n_3}\overline{\omega}_{n_3}\right)^2}\right]} \quad (23)$$

Similarly, the steady-state response of the liquid carrier under the action of a transversely concentrated excitation force can be solved:

$$u_2(x_3,t_1) = \sum_{n_4=1}^{\infty} W_{n_4}(x_3) q_{n_4}(t_1) = \sum_{n_4=1}^{\infty} \frac{F_e e^{i\left(\omega_0 t_1 - \varphi_0 - \varphi_{n_4}\right)}\sin\theta_3 W_{n_4}(x_{30}) W_{n_4}(x_3)}{\left[\overline{\omega}_{n_4}^2\sqrt{\left(1-\overline{\omega}_{n_4}^2\right)^2 + \left(2\xi_{n_4}\overline{\omega}_{n_4}\right)^2}\right]} \quad (24)$$

where $W_{n_4}(x_3)$ is a function of the bending vibration mode;$\varphi_{n_4} = \tan^{-1}\left(\frac{2\xi_{n_4}\overline{\omega}_{n_4}}{1-\overline{\omega}_{n_4}^2}\right)$; $\overline{\omega}_{n_4} = \frac{\omega_0}{\omega_{n_4}}$ is the ratio of the excitation frequency to the natural frequency of the bending vibration of the system.

When$\omega_{n_4} = \omega_0$, the bending vibration of the liquid carrier is resonant in ordern_4, and the displacement steady-state response is dominated by order n_4 vibration mode. Therefore, the displacement steady-state response can be simplified as:

$$u_2(x_3,t_1) = W_{n_4}(x_3) q_{n_4}(t_1) = \frac{F_e e^{i\left(\omega_0 t_1 - \varphi_0 - \varphi_{n_4}\right)}\sin\theta_3 W_{n_4}(x_{30}) W_{n_4}(x_3)}{\left[\overline{\omega}_{n_4}^2\sqrt{\left(1-\overline{\omega}_{n_4}^2\right)^2 + \left(2\xi_{n_4}\overline{\omega}_{n_4}\right)^2}\right]} \quad (25)$$

When studying the actual vibration at a fixed position, we can rewrite equations (23) and (25) as:

$$\begin{cases} u_1(t_1) = a_3 e^{i\left(\omega_0 t_1 - \varphi_0 - \varphi_{n_3}\right)} \\ u_2(t_1) = b_3 e^{i\left(\omega_0 t_1 - \varphi_0 - \varphi_{n_4}\right)} \end{cases} \quad (26)$$

where both a_3 and b_3 are constants, and$a_3 \neq b_3$,

$$\begin{cases} a_3 = \dfrac{F_e\cos\theta_3 W_{n_3}(x_{30}) W_{n_3}(x_3)}{\left[K_{n_3}\sqrt{\left(1-\overline{\omega}_{n_3}^2\right) + \left(2\xi_{n_3}\overline{\omega}_{n_3}\right)^2}\right]} \\ b_3 = \dfrac{F_e\sin\theta_3 W_{n_4}(x_{30}) W_{n_4}(x_3)}{\left[\overline{\omega}_{n_4}^2\sqrt{\left(1-\overline{\omega}_{n_4}^2\right)^2 + \left(2\xi_{n_4}\overline{\omega}_{n_4}\right)^2}\right]} \end{cases} \quad (27)$$

From Eq. (23) and Eq. (25), the phases of the longitudinal vibration and bending vibration are $\varphi_{n_3} = \tan^{-1}\left(\frac{2\xi_{n_3}\overline{\omega}_{n_3}}{1-\overline{\omega}_{n_3}^2}\right)$ and$\varphi_{n_4} = \tan^{-1}\left(\frac{2\xi_{n_4}\overline{\omega}_{n_4}}{1-\overline{\omega}_{n_4}^2}\right)$, respectively. For the liquid carrier, the damping of the longitudinal vibration and bending vibration is not the same, *i.e.*,$\xi_{n_3} \neq \xi_{n_4}$; bringing in the phase equation gives$\varphi_{n_3} \neq \varphi_{n_4}$. Thus, there is a phase difference between the longitudinal vibration and bending vibration with a phase difference of$\left|\varphi_{n_3} - \varphi_{n_4}\right|$. Two mutual perpendicular vibrations at the same excitation frequency with different phases meet the three conditions of micro-amplitude elliptical motion. Therefore, the particles on the tube wall undergo micro-amplitude elliptical motion, which causes the liquid in the tube to move forward. And Eq. (26) is the parametric equation of the micro-amplitude elliptical motion trajectory.

As shown in Fig. 7, when there is a phase difference between longitudinal vibration and bending vibration, the trajectory of a point on the liquid carrier wall in one cycle is elliptical. The bending and longitudinal vibrations at a point on the tube wall during one cycle are shown in Fig. 7(a), where the red line indicates the longitudinal vibration and the green line the bending vibration. The points at different moments in the motion of the elliptical trajectory are shown in Fig. 7(b). The different postures of the liquid carrier at different moments during the cycle are shown in Fig. 7(c)-Fig. 7(f).

When all the microscopic particles on the liquid carrier carry out the micro-amplitude elliptical motion as in Fig. 7, the macroscopic manifestation is that the liquid moves forward because of the frictional force from the tube wall.

3.2. Theory of liquid cavitation

The above analysis shows that the superimposition of longitudinal vibration and bending vibration in the liquid carrier causes the wall of

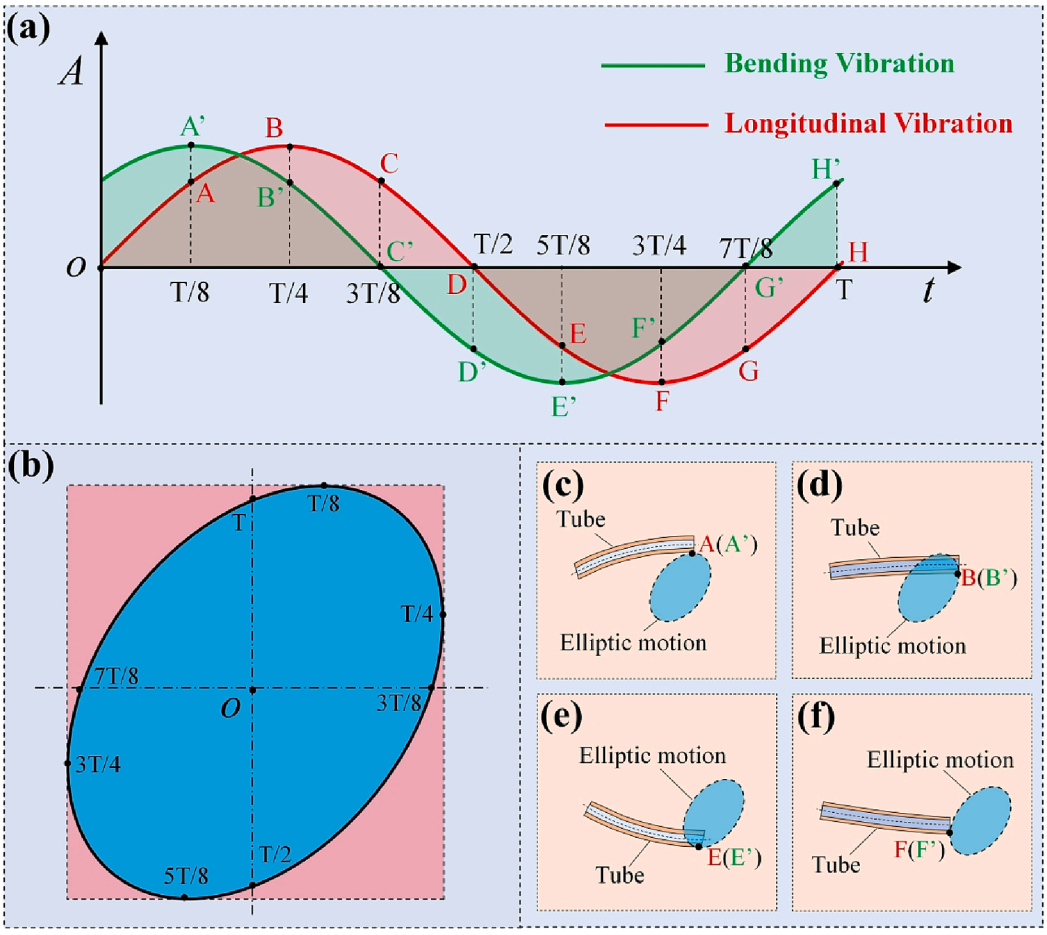

Fig. 7. Micro-amplitude elliptical motion of a point on the liquid carrier: (a) Longitudinal vibration and bending vibration of a point on the liquid carrier in a single cycle; (b) Trajectory of the micro-amplitude elliptical motion of a point on the liquid carrier; (c) The motion posture of a point on the liquid carrier at the moment A(A'); (d) The motion posture of a point on the liquid carrier at the moment B(B'); (e) The motion posture of a point on the liquid carrier at the moment E(E'); (f) The motion posture of a point on the liquid carrier at the moment F(F').

the liquid carrier to form a micro-amplitude elliptical motion, which drives the liquid to move. The longitudinal vibration and bending vibration are analyzed separately to allow a clear analysis of liquid cavitation.

Cavitation theory suggests that a threshold value of sound intensity is required to produce cavitation [66,67], and the formula for calculating the cavitation threshold can be expressed as follows:

$$P_B = P_0 - P_V + \frac{2}{3\sqrt{3}}\sqrt{\frac{\left(\frac{2\sigma}{R_0}\right)^3}{\left(P_0 - P_V + \frac{2\sigma}{R_0}\right)}} \tag{28}$$

where P_0 is the static pressure in the liquid; P_V is the vapor pressure inside the bubble; σ is the surface tension coefficient; and R_0 is the radius of the cavitation nucleus (radius of the bubble).

The above equation is complex, and an empirical formula can be used instead of the formula for the cavitation threshold:

$$P_B = 0.8(1g\eta + 5) \tag{29}$$

where η is viscosity of the liquid.

As seen from Eq. (29), the cavitation threshold is higher for high-viscosity liquids. This is because the viscous liquid layer inhibits cavitation events more significantly at higher liquid viscosities. However, as energy continues to be supplied, eventually the viscosity liquid layer is unable to suppress cavitation, and the powerful impact created by the collapse of the cavitation nucleus releases a large amount of energy in a very short time, prompting the liquid on the surface of the atomized end to overcome surface tension and form droplets that escape into the air.

From the above vibration analysis, the acceleration can be found by taking the second derivative of the displacement steady-state response with respect to time. Supposing that the mass of a point ism_2, its acceleration in the longitudinal vibration displacement steady-state response can be denoted:

$$\frac{\partial^2 u_1(x_3,t_1)}{\partial t_1^2} = -\omega_0^2 \frac{F_e\cos\theta_3 e^{i\left(\omega_0 t_1-\varphi_0-\varphi_{n_3}\right)} W_{n_3}(x_{30}) W_{n_3}(x_3)}{\left[K_{n_3}\sqrt{\left(1-\overline{\omega}_{n_3}^2\right)+\left(2\xi_{n_3}\overline{\omega}_{n_3}\right)^2}\right]} \tag{30}$$

Then, the force at this point under the steady-state response of the longitudinal vibration displacement can be expressed as follows:

$$f_{u_1} = -\omega_0^2 m_2 \frac{F_e\cos\theta_3 e^{i\left(\omega_0 t_1-\varphi_0-\varphi_{n_3}\right)} W_{n_3}(x_{30}) W_{n_3}(x_3)}{\left[K_{n_3}\sqrt{\left(1-\overline{\omega}_{n_3}^2\right)+\left(2\xi_{n_3}\overline{\omega}_{n_3}\right)^2}\right]} \tag{31}$$

Its acceleration in the bending vibration displacement steady-state response can be expressed as follows:

$$\frac{\partial^2 u_2(x_3,t_1)}{\partial t_1^2} = -\omega_0^2 \frac{F_e\sin\theta_3 e^{i\left(\omega_0 t_1-\varphi_0-\varphi_{n_4}\right)} W_{n_4}(x_{30}) W_{n_4}(x_3)}{\left[\overline{\omega}_{n_4}^2\sqrt{\left(1-\overline{\omega}_{n_4}^2\right)+\left(2\xi_{n_4}\overline{\omega}_{n_4}\right)^2}\right]} \tag{32}$$

Then, the force at this point in the bending vibration displacement steady-state response can be expressed as follows:

$$f_{u_2} = -\omega_0^2 m_2 \frac{F_e\sin\theta_3 e^{i\left(\omega_0 t_1-\varphi_0-\varphi_{n_4}\right)} W_{n_4}(x_{30}) W_{n_4}(x_3)}{\left[\overline{\omega}_{n_4}^2\sqrt{\left(1-\overline{\omega}_{n_4}^2\right)+\left(2\xi_{n_4}\overline{\omega}_{n_4}\right)^2}\right]} \tag{33}$$

Eq. (31) and Eq. (33) are the forces at any point of the liquid carrier. Knowing the force on the wall of the tube, the force on the liquid inside

the liquid carrier can be analyzed, and when the force on the liquid reaches the cavitation threshold, the liquid produces cavitation, and atomization is achieved.

4. Results and discussion

4.1. Analysis of impedance

The frequency range for the impedance analysis was 300–800 kHz. Impedance measurements were performed on the FTICA under six conditions, no load and loaded liquid viscosities of 50 cP, 75 cP, 100 cP, 125 cP and 150 cP. The results are shown in Fig. 8(a) - Fig. 8(f).

The minimum impedance value at no load occurs at 694 kHz, as shown in Fig. 8(a). The impedance minimum occurs at 696 kHz when the liquid passes through. The difference between the two cases is 2 kHz. As the fluid viscosity changes, the minimum impedance value remains the same, which indicates that the resonant frequency of the FTICA does not change with the viscosity of the liquid. Therefore, the data presented in Fig. 8(b) - Fig. 8(f) basically overlap. In this study, eight resonant frequency points were selected as possible target frequencies for atomization based on the results of impedance analysis; these frequencies were 326 kHz, 392 kHz, 420 kHz, 507 kHz, 567 kHz, 606 kHz, 648 kHz, 696 kHz and 714 kHz.

4.2. Atomization rate and atomized particle sizes

Note: The center of the connecting block is eccentric to the center of the metal substrate; the viscosity of the atomizing liquid is 50 cP; the atomizer is driven at 85 V.

Atomization experiments were performed with a fluid with a viscosity of 50 cP for the eight resonant frequencies selected from the impedance analysis results. The atomization results are shown in Table 3.

The best atomization effect is obtained at 507 kHz. Thus, this frequency was selected as the driving frequency for the subsequent atomization measurement experiments. In the experiments, liquids with six different viscosities were used for atomization. For each viscosity, the driving voltage was increased from 65 V to 85 V, and 11 sets of atomization measurements were taken at 2 V intervals. The experimental results are shown in Fig. 9(a).

It is showed that the proposed FTICA can atomize liquids with viscosities up to 175 cP. When the driving voltage is constant, the atomization rate decreases with increasing viscosity. When the viscosity is constant, the atomization rate increases with increasing driving voltage. To express the atomization effect of this FTICA more visually, selected atomization photos for each viscosity at 85 V drive voltage are shown in

Table 3
Atomization at different resonance frequencies.

Resonant Frequency	Atomization	Atomization flow rate (mg/min)
326 kHz	No	0
392 kHz	No	0
420 kHz	No	0
507 kHz	Yes	56.35
567 kHz	No	0
606 kHz	No	0
648 kHz	Yes	16.22
696 kHz	No	0
714 kHz	No	0

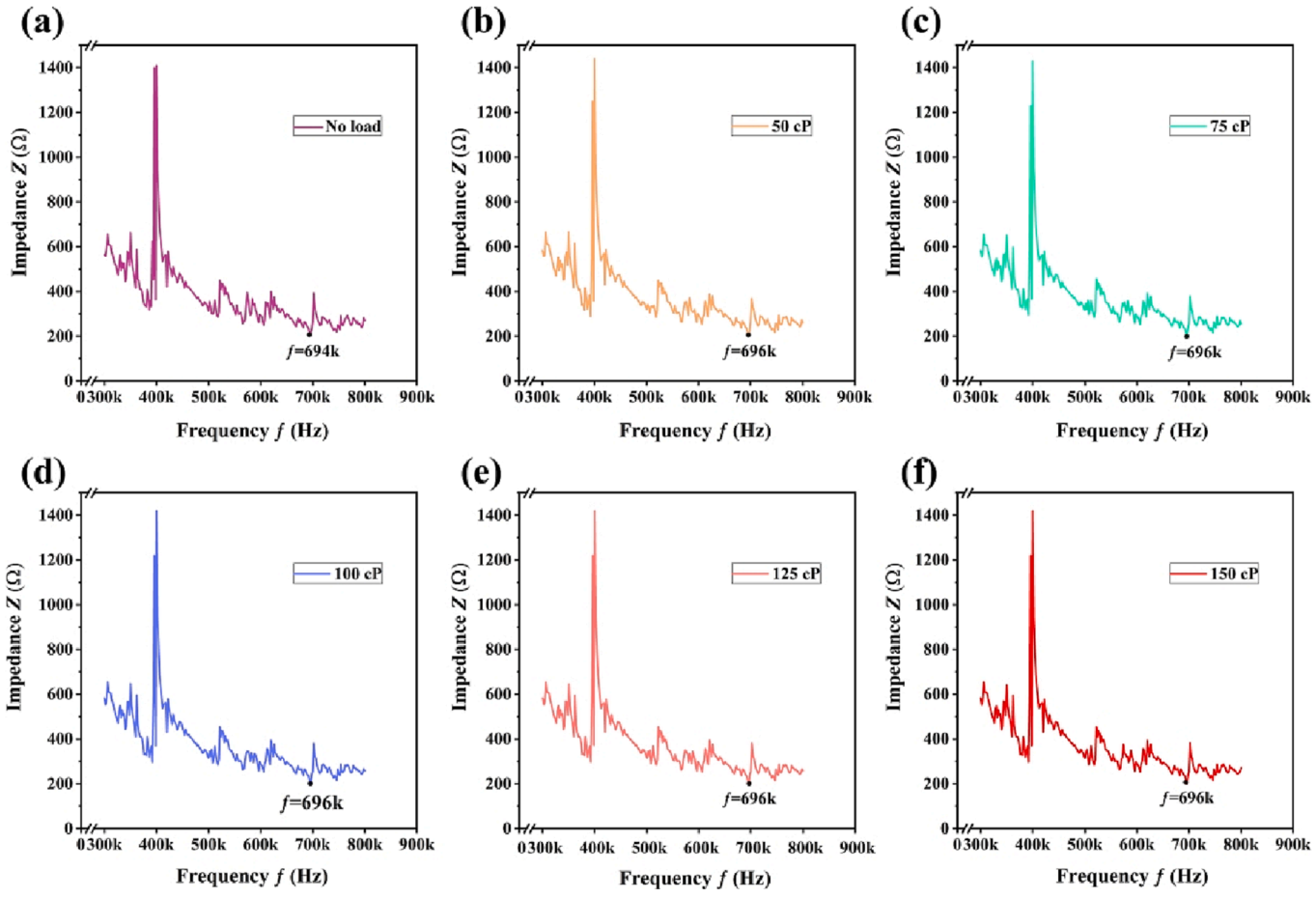

Fig. 8. Impedance measurements for liquids with different viscosities: (a) No load; (b) 50 cP; (c) 75 cP; (d) 100 cP; (e) 125 cP; (f) 150 cP.

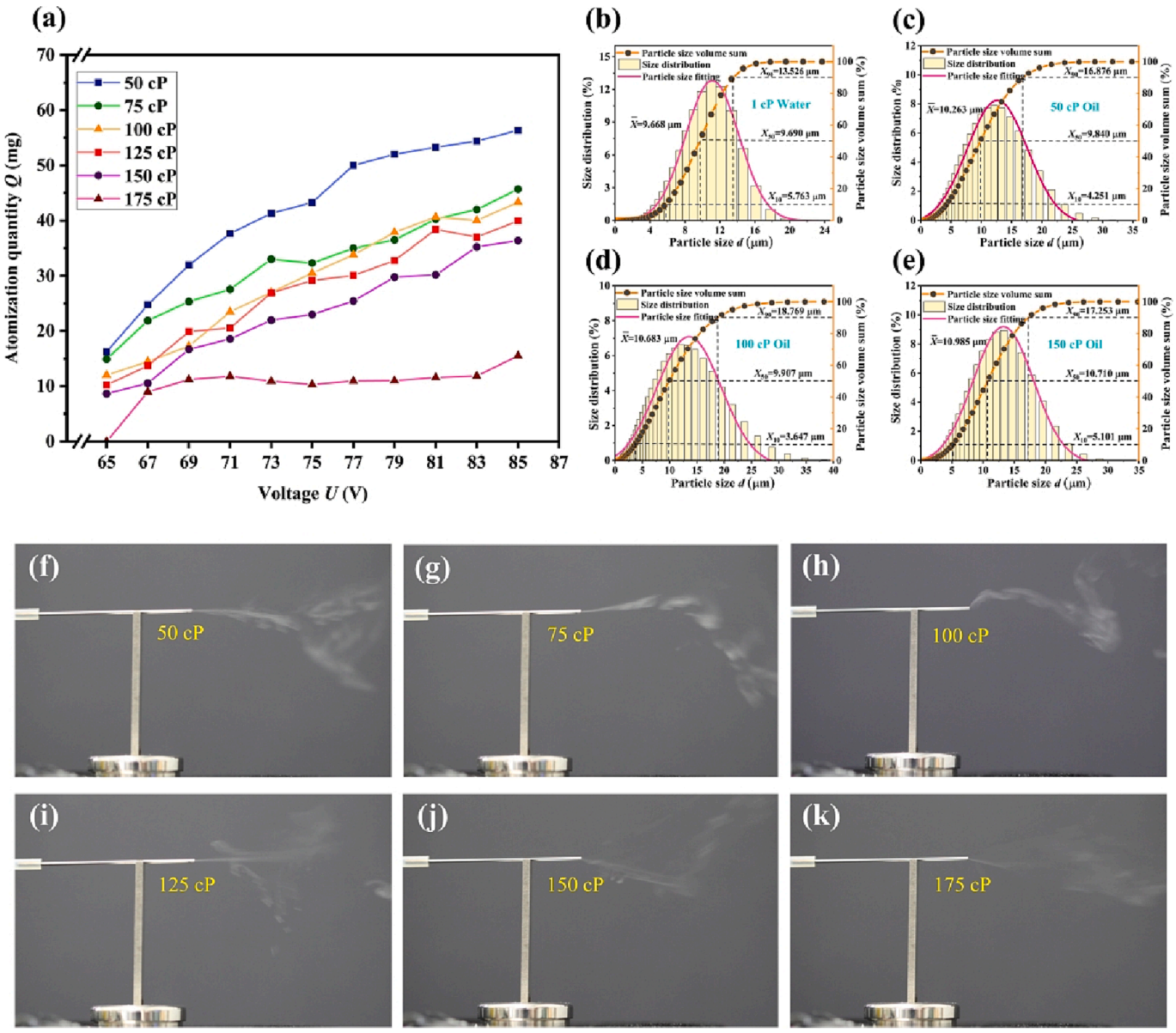

Fig. 9. Atomization experimental data: (a) Relationship between the atomization rate and driving voltage for liquids with different viscosities at a driving frequency of 507 kHz; (b) Distribution of atomized particle diameter for a liquid with a dynamic viscosity of 1 cP; (c) Distribution of atomized particle diameter for a liquid with a dynamic viscosity of 50 cP; (d) Distribution of atomized particle diameter for a liquid with a dynamic viscosity of 100 cP; (e) Distribution of atomized particle diameter for a liquid with a dynamic viscosity of 150 cP; (f) The atomization effect of a liquid with a dynamic viscosity of 50 cP; (g) The atomization effect of a liquid with a dynamic viscosity of 75 cP; (h) The atomization effect of a liquid with a dynamic viscosity of 100 cP; (i) The atomization effect of a liquid with a dynamic viscosity of 125 cP; (j) The atomization effect of a liquid with a dynamic viscosity of 150 cP; (k) The atomization effect of a liquid with a dynamic viscosity of 175 cP.

Fig. 9(f) - Fig. 9(k).

The atomized particle diameters of the four liquids with viscosities of 1 cP, 50 cP, 100 cP and 150 cP are normally distributed, the mean values of the atomized particles are 9.668 μm, 10.263 μm, 10.683 μm and 10.985 μm, and 50% of the particles are smaller than 9.690 μm, 9.840 μm, 9.907 μm and 10.710 μm, respectively, as shown in Fig. 9(b) - Fig. 9(e). There is a small increase in the average particle size with increasing viscosity, but the increase in diameter is only approximately 10% for a liquid with a viscosity of 150 cP compared to that of distilled water with a viscosity of 1 cP. The experiments show that the FTICA can effectively atomize liquids with viscosities up to 150 cP, with particle sizes of approximately 10 μm under 507 kHz, 85 V driving conditions.

4.3. Vibration displacement measurement of the FTICA

A spectral analysis of the displacement measurements of the vibration source was carried out, where the three resonant frequencies of 507 kHz, 605 kHz and 718 kHz are identified, and the displacement distribution corresponding to these frequencies at the time of maximum displacement is shown in Fig. 10(a) - Fig. 10(c). The results show that in the atomization experiment, the FTICA can achieve atomization when the driving frequency is 507 kHz, but the FTICA cannot achieve atomization when the driving frequency is 605 kHz or 718 kHz. Therefore, when the connecting block is at the maximum vibration displacement position, the vibration can be better transmitted, and atomization occurs in the liquid carrier, as shown in Fig. 10(a). If the connecting block is in a position where there is no vibration or the amplitude is small, as shown in Fig. 10(b) and Fig. 10(c), then the connecting block does not transmit

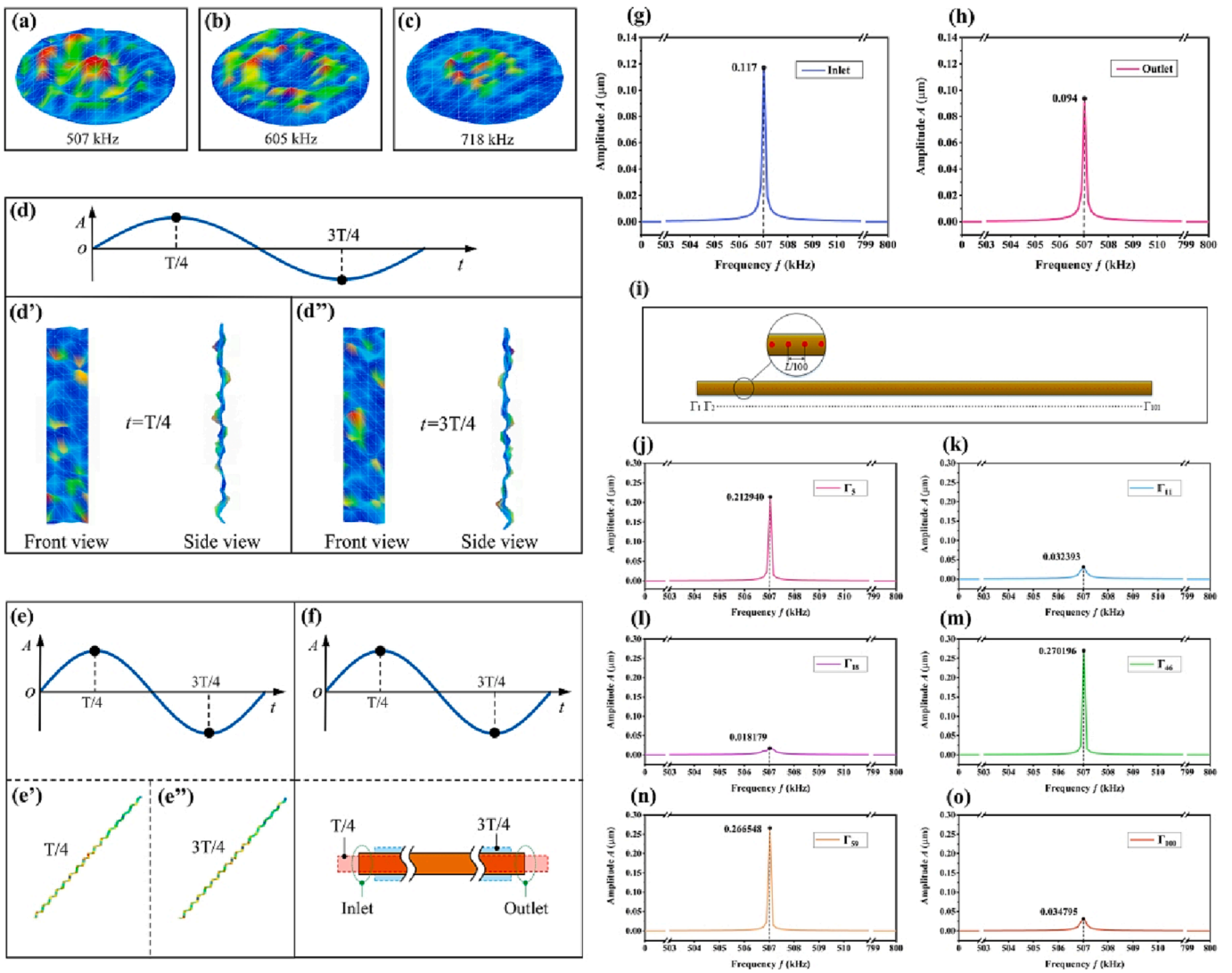

Fig. 10. Vibration experimental data: (a) Displacement distribution of the vibration source at the moment of maximum displacement at 507 kHz resonance frequency; (b) Displacement distribution of the vibration source at the moment of maximum displacement at 605 kHz resonance frequency; (c) Displacement distribution of the vibration source at the moment of maximum displacement at 718 kHz resonance frequency; (d) Displacement distribution of the connecting block at the moment of maximum displacement; (d') Displacement distribution of the connecting block at the moment T/4; (d'') Displacement distribution of the connecting block at the moment 3 T/4; (e) Displacement distribution of the liquid carrier at the moment of maximum displacement; (e') At the moment of T/4, distribution of bending vibration displacement of the liquid carrier synthesized from 101 measurements; (e'') At the moment of 3 T/4, distribution of bending vibration displacement of the liquid carrier synthesized from 101 measurements; (f) Schematic diagram of the longitudinal vibration displacement of the liquid carrier; (g) Longitudinal vibration displacement of the end face of the inlet end of the liquid carrier; (h) Longitudinal vibration displacement of the end face of the atomization end of the liquid carrier; (i) Distribution of liquid carrier bending vibration displacement measurement points; (j) Vibration displacement of point Γ_5; (k) Vibration displacement of point Γ_{11}; (l) Vibration displacement of point Γ_{18}; (m) Vibration displacement of point Γ_{46}; (n) Vibration displacement of point Γ_{59}; (o) Vibration displacement of point Γ_{100}.

vibration, and subsequent atomization in the liquid carrier is not possible. Therefore, it is necessary to design the structure so that the connecting block is located at the maximum displacement position of the vibration source to achieve atomization.

As the vibrations transmitted from the vibration source to the connecting block at 606 kHz and 718 kHz are too small to form resonance, the connecting block is analyzed in terms of vibrational displacements only at 507 kHz, and the distribution of displacements at the time of maximum displacement is shown in Fig. 10(d). The Figure represents the displacement distribution at the time of maximum displacement in the forward and backward directions within one cycle, where Fig. 10(d') shows the moment of maximum displacement in the forward direction and Fig. 10(d'') shows the moment of maximum displacement in the backward direction. For a clearer representation, the front and side views are shown in both Figures. When the connecting block is mounted eccentrically on a vibration source, the connecting block is subjected to a tilting force that drives it to vibrate out-of-plane, thus, when a single signal is input, it causes longitudinal and bending vibrations of the liquid carrier.

Due to the limitations of the measurement tool, only the displacements at the inlet and outlet ends of the liquid carrier in the direction of the axis were measured in this study to demonstrate the presence of longitudinal displacements. As shown in Fig. 10(g) - Fig. 10(h), the peak displacement at the inlet end is 0.117 μm, and the peak displacement at the atomization end is 0.094 μm.

Fig. 10(e) - Fig. 10(f) shows the vibration displacement of the liquid carrier. Fig. 10(e) shows the distribution of the bending vibration displacement of the liquid carrier synthesized from 101 measurements, which shows that the liquid carrier bending vibration mode is the 30th order vibration at 507 kHz excitation. Fig. 10(f) shows a schematic

diagram of the longitudinal vibration displacement of the liquid carrier obtained on the basis of the above experiments, where the orange part indicates the shape of the liquid carrier without vibration and the red part and blue part indicate the tensile shape and compressive shape of the longitudinal vibration of the liquid carrier.

In the bending vibration experiment, a precision displacement stage was used to adjust the vibration measurement position in steps of 0.5 mm. The vibration displacements at a 507 kHz driving frequency were measured uniformly in the direction of the liquid carrier axis at 101 points, denoted by $\Gamma_1, \Gamma_2, \Gamma_3, \ldots\ldots, \Gamma_{101}$, as shown in Fig. 10(i). Fig. 10(j) - Fig. 10(o) show the experimental data at points $\Gamma_5, \Gamma_{11}, \Gamma_{18}, \Gamma_{46}, \Gamma_{59}$ and Γ_{100}. The maximum displacement of the liquid carrier is approximately 0.27 μm, and the minimum displacement is approximately 0.018 μm, which can be considered to be near the node. The fact that the peak displacement of the liquid carrier bending vibration is higher than that of the liquid carrier longitudinal vibration further demonstrates that longitudinal vibration is more difficult to excite than bending vibration.

The above experiment proved that the vibration of the vibration

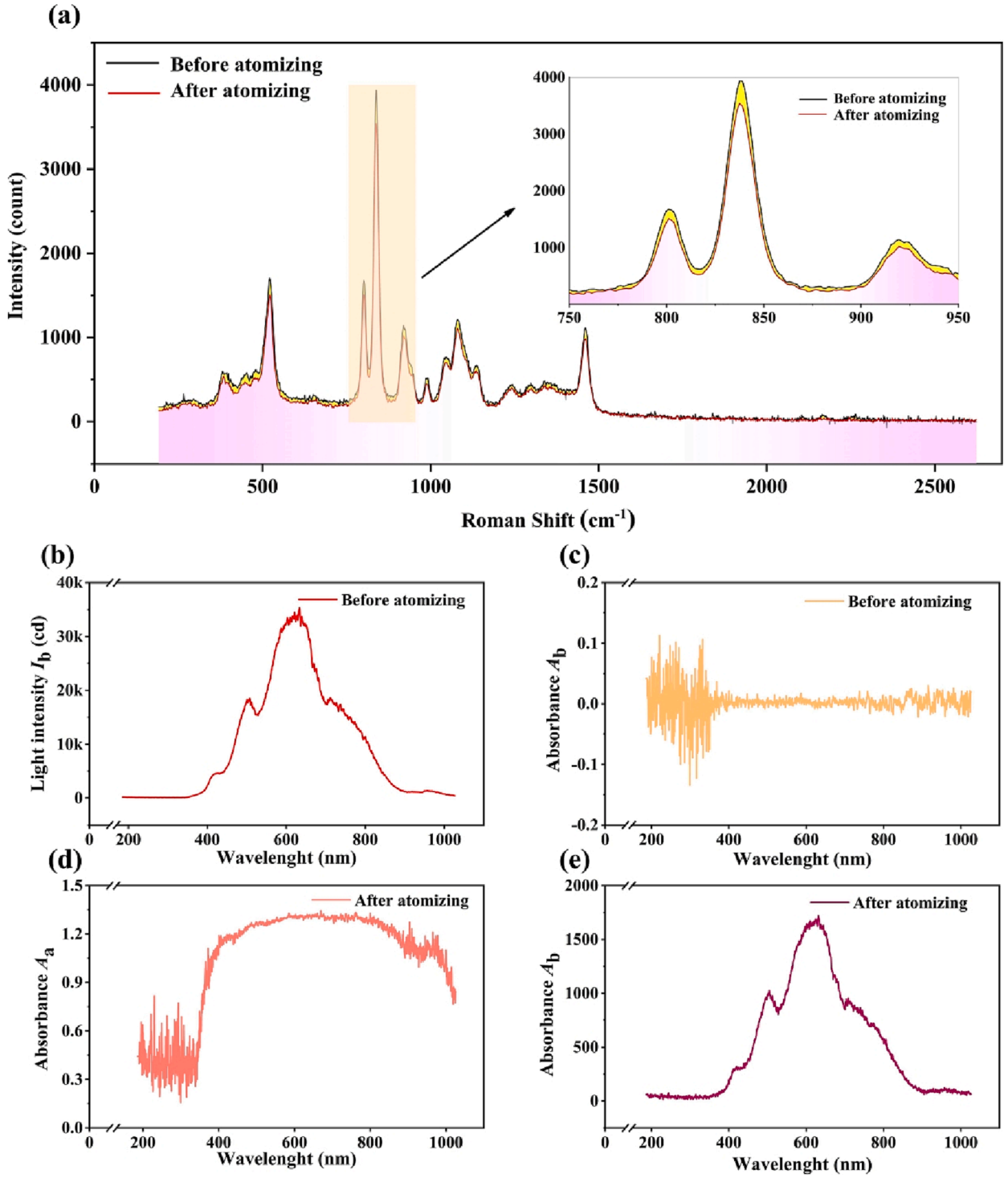

Fig. 11. Spectroscopic experimental data: (a) Raman spectra of the liquid before and after atomization; (b) Light intensity before atomization; (c) Absorbance before atomization; (d) Absorbance after atomization; (e) Light intensity after atomization.

source is transmitted to the liquid carrier by the connecting block, which causes longitudinal vibration and bending vibration in the liquid carrier. The synthesis of the vibrations in both directions causes the particles on the inside of the liquid carrier to move elliptically, thus prompting the liquid inside the liquid carrier to move toward the atomization end under micro-amplitude elliptical motion conditions. Meanwhile, due to the longitudinal vibration and bending vibration constantly pulling and pressing the liquid, liquid cavitation occurs due to the dissolved fraction of air. When the liquid reaches the atomization end, due to the instantaneous explosive force of cavitation breaking the continuity of the liquid, the liquid at the end escapes into the air at high speed as tiny particle droplets, thus achieving atomization. This is also consistent with the theoretical derivation of the micro-amplitude elliptical motion, and the actual elliptical motion trajectory can be finally obtained according to the experimental measured data.

4.4. Spectral analysis of atomized liquids

The phenomenon of cavitation is an important mechanism for achieving atomization with the proposed FTICA. Therefore, this section presents our investigation of the changes that occur in the atomized liquid inside the liquid carrier by Raman spectroscopy and absorbance experiments with full wavelength light.

First, Raman spectroscopy was used to verify whether the molecular structure of the liquid changes from before to after atomization. Propylene glycol liquid with a viscosity of 50 cP was used for the experiments. The original propylene glycol liquid before atomization and liquid obtained by collecting droplets after atomization were placed on slides. The results of Raman spectroscopy analysis of both are shown in Fig. 11(a).

The spectral peaks at different positions in the diagram represent different functional groups, and the intensities of the peaks represent the concentrations of functional groups. The Raman spectral peaks of the liquids before and after atomization were identical, indicating that the two were the same substance and that the FTICA achieved atomization through a physical mechanism. In addition, the spectral intensity of the liquid before atomization is slightly higher than that after atomization, as shown by the black and red curves in Fig. 11(a), respectively, indicating that the concentration of functional groups in the liquid before atomization is higher than the concentration of functional groups after atomization, which is the result of a small number of droplets drifting into the air when the droplets are collected after atomization. This experiment shows that the degree of cavitation of the liquid after vibration, although intense, does not reach the molecular level, and therefore, no new substances are produced by the atomization. The FTICA can achieve atomization in the physical sense and meets the basic requirements of an ultrasonic atomizer.

In the second experiment, a high-power light source transmitter and receiver was used to analyze the absorbance and light intensity of the liquid before and after atomization. The experiment was carried out using propylene glycol liquid with a viscosity of 50 cP.

We assume that the light intensities at the receiving end of the light source before and after atomization are I_b and I_a, respectively, and define the absorbance coefficient after atomization as:

$$A_a = \lg \frac{I_b}{I_a} \tag{34}$$

Due to the constant light intensity at the receiving end before atomization, the absorbance before atomization should be$A_b = \lg \frac{I_b}{I_b} = 0$. The experimental results are shown in Fig. 11(b) - Fig. 11(e). Fig. 11(b) shows the light intensity I_b distribution at the receiving end after passing through the liquid before the FTICA is turned on. Fig. 11(c) shows the absorbance before atomization A_b, the fluctuations of which demonstrate the systematic errors introduced into the instrument by environmental factors. The absorbance after atomization A_a is shown in Fig. 11(d). The Raman spectroscopy experiments show that the atomization does not produce new material, so the difference in absorbance in Fig. 11(c) and Fig. 11(d) is due to the cavitation of the gas originally dissolved in the liquid caused by the high pressure generated during the vibration of the FTICA. Using Eq. (34) and the light intensity before and absorbance after atomization, I_b and A_a, measured in the experiment, the light intensity after atomization I_a can be calculated, and the distribution is shown in Fig. 11(e). The occurrence of cavitation in the FTICA leads to the creation of a large amount of tiny bubbles. During the creation and collapse of these small bubbles, the liquid is atomized, and more light is absorbed and reflected, so the light intensity at the receiving end is reduced and the absorption in the atomization is increased. This experiment demonstrates the presence of liquid cavitation during the atomization process.

4.5. Comparison with conventional ultrasonic atomizers

To discuss and demonstrate the advantages and disadvantages of the FTICA in this study, we compared it with a variety of conventional ultrasonic atomizers and show in Table 4.

Analyzing Table 4, we can know that compared to the conventional ultrasonic atomizer, the FTICA in this study is able to atomize high-viscosity liquids without parameter optimization and control the size of atomized particle diameter. This is its most obvious advantage.

At present, because the parameters of the FTICA in this study have not been optimized, it has a smaller atomization rate than other ultrasonic atomizers. However, we believe that the deficiency can be overcome in the subsequent optimization experiments.

5. Conclusion

In this study, we propose a novel atomization mechanism that uses two coupled vibrations to induce micro-amplitude elliptical motion of the particles on the surface of the liquid carrier, which produces a similar effect as localized traveling waves to push the liquid forward and induce cavitation to achieve atomization. A prototype was designed and built to atomize liquids with a maximum viscosity of 175 cP at room temperature, with a maximum atomization rate of 56.35 mg/min and an average particle diameter of approximately 10 μm. A vibration model based on a three-part structure with a circular base, a rectangular plate and a needle-shaped through-tube for coupled atomization modes was developed. The vibration displacements of the components of the

Table 4
Comparison with conventional ultrasonic atomizers.

Type	Advantage	Disadvantage	Maximum atomizing viscosity
SAW atomizer	Large atomizing volume. Simple structure.	Energy utilization rate is low. The droplet size can- not be controlled. The particle size distribution of the droplets is not concentrated.	About 30 cP
Static mesh atomizer	Atomization process is controllable. The droplets are evenly distributed.	Complex structure	
Dynamic mesh atomizer	Simple structure. High energy utilization.	Low viscosity of atomized liquid	
FTICA	High viscosity of atomized liquid. Simple structure. The droplet size can be controlled. The droplets are evenly distributed.	Low atomizing rate	175 cP

atomized prototype were measured using a 3D Doppler vibrometer at a frequency of 507 kHz, which showed that the vibration mode of the atomized structure was of order 30 and that the theoretical solution was of order 26, where the error was approximately 15%.

It was postulated that the longitudinal and bending vibrations of the needle-through-tube led to the cavitation effect of the liquid inside it and thus to atomization. Based on cavitation theory, a force-based model of the inner wall of the needle-type tube and its cavitation threshold were developed. A Raman spectroscopy experiment was used to verify that there were no changes in the chemical properties of the liquid before and after atomization, and an absorption spectroscopy experiment was used to demonstrate the occurrence of cavitation, verifying the conjecture that cavitation causes atomization.

This study proposes a new mechanism for high-viscosity physical atomization, offering new possibilities for transpulmonary inhalation therapy, engine fuel supply, solid-state battery processing and other areas requiring high-viscosity microparticles. In subsequent studies, the current structural parameters will be further optimized, and the atomization performance at driving frequencies above 800 kHz will be further investigated.

CRediT authorship contribution statement

Tang Xie: Methodology, Formal analysis, Writing – original draft. **Yaohua Zeng:** Methodology, Investigation, Writing – original draft. **Zhenzhen Gui:** Writing – review & editing. **Mingdong Ma:** Investigation. **Yuxuan Huo:** Investigation. **Weirong Zhang:** Validation. **Tian Tan:** Investigation. **Tao Zou:** Conceptualization, Methodology. **Fan Zhang:** Formal analysis, Writing – review & editing. **Jianhui Zhang:** Conceptualization, Methodology, Supervision.

Declaration of Competing Interest

The authors declare that they have no known competing financial interests or personal relationships that could have appeared to influence the work reported in this paper.

Acknowledgements

This work was supported by National Natural Science Foundation of China (Grant No. 51705093), Guangdong Basic and Applied Basic Research Foundation (Grant No. 2019B1515120017, 2022A1515010265 and 2020A1515110619), Science and Technology Program of Guangzhou (Grant No. 202201020158 and 202201020191), The Graduate-Ability-Promotion Plan of Guangzhou University (Granted No. 2022GDJC-M21). And we thank Sunny Optical Intelligence Technology Co.,Ltd. for providing the vibration measurement equipment and for helping with the vibration measurement experiments, and Optosky (Xiamen) Photonics Inc. for providing the spectroscopic measurement equipment and help with the spectroscopic measurement experiments. We also thank Professor Jiamei Jin of Nanjing University of Aeronautics and Astronautics for his theoretical guidance.

Appendix A. Supplementary data

Supplementary data to this article can be found online at https://doi.org/10.1016/j.ultsonch.2023.106331.

References

[1] T.D. Donnelly, J. Hogan, A. Mugler, N. Schommer, M. Schubmehl, A.J. Bernoff, An experimental study of micron-scale droplet aerosols produced via ultrasonic atomization, Phys. Fluids 16 (8) (2004), https://doi.org/10.1063/1.1759271.
[2] R. Rajan, A.B. Pandit, Correlations to predict droplet size in ultrasonic atomization, Ultrasonics 39 (4) (2001) 235–255, https://doi.org/10.1016/S0041-624X(01)00054-3.
[3] J. Zhang, Q. Yan, W. Sun, Advances in piezoelectric atomizers, Trans. Nanjing Univ. Aeronaut. Astronaut. 37 (1) (2020) 54–69, https://doi.org/10.16356/j.1005-1120.2020.01.005.
[4] M.N. Topp, P. Eisenklam, Industrial and medical uses of ultrasonic atomizers, Ultrasonics 10 (3) (1972) 127–133, https://doi.org/10.1016/0041-624X(72)90009-1.
[5] F. Lacas, P. Versaevel, P. Scouflaire, G. Coeur-Joly, Design and performance of an ultrasonic atomization system for experimental combustion applications, Part. Part. Syst. Char. 11 (2) (1994) 166–171, https://doi.org/10.1002/ppsc.19940110210.
[6] S.P. Newman, S.W. Clarke, Therapeutic aerosols 1–physical and practical Considerations, Thorax 38 (12) (1983) 881, https://doi.org/10.1136/thx.38.12.881.
[7] H. Okawa, K. Nishi, Y. Kawamura, T. Kato, K. Sugawara, Utilization of ultrasonic atomization for dust control in underground mining, Jpn. J. Appl. Phys. 56 (7S1) (2017) 07JE10, https://doi.org/10.7567/JJAP.56.07JE10.
[8] S. Ro, R. Imai, A. Kitamura, T. Jinta, N. Nishimura, Ultrasonic humidifier lung as a mimic of COVID-19, Respirol. Case Rep. 9 (6) (2021) e00761.
[9] R.W. Wood, A.L. Loomis, The physical and biological effects of high-frequency sound-waves of great intensity, The London, Edinburgh, and Dublin Philosoph. Mag. J. Sci. 4 (22) (1927) 417–436, https://doi.org/10.1080/14786440908564348.
[10] R.M. White, F.W. Voltmer, Direct piezoelectric coupling to surface elastic waves, Appl. Phys. Lett. 7 (12) (1965) 314–316, https://doi.org/10.1063/1.1754276.
[11] D. Sun, K. F. Böhringer, M. Sorensen, E. Nilsson, D. R. Goodlett, Droplet Delivery Control for Surface Acoustic Wave Nebulization Mass Spectrometry. In: 2019 20th International Conference on Solid-State Sensors, Actuators and Microsystems & Eurosensors XXXIII (TRANSDUCERS & EUROSENSORS XXXIII), 2019, pp. 49-52. https://doi.org/10.1109/TRANSDUCERS.2019.8808244.
[12] T. Nakamoto, S. Ollila, S. Kato, H. Li, G. Qi, Enhancement Method of Surface Acoustic Wave-Atomizer Efficiency for Olfactory Display, J. Vis. Exp. 141 (2018) e58409.
[13] B. De Heij, B. van der Schoot, N. F. de Rooij, H. Bo, J. Hess, Modelling and Optimisation of a vaporiser for inhalation drug therapy. In: Proceedings of the Second International Conference on Modelling and Simulation of Microsystems, 1999, pp. 542-545.
[14] G.H. Wang, Z.Y. Zhou, S.M. Yuan, C.G. Liu, Theoretical and experimental analysis of droplet characteristics in piezoelectrically actuated microjet, J. Chin. Sci. Instrum 23 (2002) 6–8, https://doi.org/10.19650/j.cnki.cjsi.2002.s3.003.
[15] Y.R. Jeng, C.C. Su, G.H. Feng, Y.Y. Peng, An investigation into a piezoelectrically actuated nebulizer with μEDM-made micronozzlearra, Exp. Therm Fluid Sci. 31 (8) (2007) 1147–1156, https://doi.org/10.1016/j.expthermflusci.2006.12.001.
[16] N. Maehara, S. Ueha, E. Mori, Influence of the vibrating system of a multipinhole-plate ultrasonic nebulizer on its performance, Rev. Sci. Instrum. 57 (11) (1986) 2870–2876, https://doi.org/10.1063/1.1139006.
[17] Q. Yan, C. Wu, J. Zhang, Effect of the dynamic cone angle on the atomization performance of a piezoceramic vibrating mesh atomizer, Appl. Sci. 9 (9) (2019) 1836, https://doi.org/10.3390/app9091836.
[18] M. Shafaee, S. Mahmoudzadeh, Numerical investigation of spray characteristics of an air-blast atomizer with dynamic mesh, Aerosp. Sci. Technol. 70 (2017) 351–358, https://doi.org/10.1016/j.ast.2017.08.024.
[19] R.J. Lang, Ultrasonic atomization of liquids, J. Acoust. Soc. Am. 34 (1) (1962) 6–8, https://doi.org/10.1121/1.1909020.
[20] R.R. Perron, The design and application of a reliable ultrasonic atomizer, IEEE Trans. Sonics Ultrason. 14 (4) (1967) 149–152, https://doi.org/10.1109/T-SU.1967.29430.
[21] J. Kim, J.J. Kim, S.J. Lee, Efficient removal of indoor particulate matter using water microdroplets generated by a MHz-frequency ultrasonic atomizer, Build. Environ. 175 (2020), 106797, https://doi.org/10.1016/j.buildenv.2020.106797.
[22] G. Percin, B.T. Khuri-Yakub, Piezoelectrically actuated flextensional micromachined ultrasound transducers. II. Fabrication and experiments, IEEE Trans. Ultrason. Ferroelectr. Freq. Control 49 (5) (2002) 585–595, https://doi.org/10.1109/TUFFC.2002.1002457.
[23] H.Y. Tseng, H.L. Lin, H.S. Chiang, In vitro evaluation of aerosol delivery by hand-held mesh nebulizers in an adult spontaneous breathing lung model, J. Aerosol Med. Pulm. Drug Deliv. 35 (2) (2022) 83–90, https://doi.org/10.1089/jamp.2021.0010.
[24] S. Wu, J. Huang, Z. Zhang, J. Wu, J. Zhang, W. Chen, Safety, tolerability, and immunogenicity of an aerosolised adenovirus type-5 vector-based COVID-19 vaccine (Ad5-nCoV) in adults: preliminary report of an open-label and randomised phase 1 clinical trial, Lancet Infect. Dis. 21 (12) (2021) 1654–1664, https://doi.org/10.1016/S1473-3099(21)00396-0.
[25] S.N. Eliseeva, E.V. Shkreba, M.A. Kamenskii, E.G. Tolstopjatova, R. Holze, V. V. Kondratiev, Effects of conductive binder on the electrochemical performance of lithium titanate anodes, Solid State Ion. 333 (2019) 18–29, https://doi.org/10.1016/j.ssi.2019.01.011.
[26] A. Cushing, T. Zheng, K. Higa, G. Liu, Viscosity analysis of battery electrode slurry, Polymers 13 (22) (2021) 4033, https://doi.org/10.3390/polym13224033.
[27] K.M. Kim, W.S. Jeon, I.J. Chung, S.H. Chang, Effect of mixing sequences on the electrode characteristics of lithium-ion rechargeable batteries, J. Power Sources 83 (1–2) (1999) 108–113, https://doi.org/10.1016/S0378-7753(99)00281-5.
[28] W.H. Finlay, C.F. Lange, M. King, D.P. Speert, Lung delivery of aerosolized dextran, Am. J. Respir. Crit. Care Med. 161 (1) (2000) 91–97, https://doi.org/10.1164/ajrccm.161.1.9812094.
[29] P. Zhang, X. Su, H. Chen, L. Geng, X. Zhao, Assessing fuel properties effects of 2, 5-dimethylfuran on microscopic and macroscopic characteristics of oxygenated fuel/

diesel blends spray, Sci. Rep. 10 (1) (2020) 1–12, https://doi.org/10.1038/s41598-020-58119-y.
[30] P. Boggavarapu, R.V. Ravikrishna, A review on atomization and sprays of biofuels for IC engine applications, Internat. J. Spray Combust. Dyn. 5 (2) (2013) 85–121, https://doi.org/10.1260/1756-8277.5.2.85.
[31] P. Boggavarapu, R. V. Ravikrishna, A comparison of jatropha methyl ester and diesel non-evaporating sprays. In: 12th international conference on liquid atomization and spray systems, 2012.
[32] D. Deshmukh, A.M. Mohan, T.N.C. Anand, R.V. Ravikrishna, Spray characterization of straight vegetable oils at high injection pressures, Fuel 97 (2012) 879–883, https://doi.org/10.1016/j.fuel.2012.01.078.
[33] Z.Y. Wu, L. Deng, J.T. Li, Q.S. Huang, Y.Q. Lu, J. Liu, S.G. Sun, Multiple hydrogel alginate binders for Si anodes of lithium-ion battery, Electrochim. Acta 245 (2017) 371–378, https://doi.org/10.1016/j.electacta.2017.05.094.
[34] A. Lozano, J.A. Garcia, J.L. Navarro, E. Calvo, F. Barreras, Influence of viscosity on droplet size distribution and generation rate in ultrasonic atomization, Atomization Sprays 20 (11) (2010), https://doi.org/10.1615/AtomizSpr.v20.i11.10.
[35] J. Law, K.W. Kong, H.Y. Chan, W. Sun, W.J. Li, E.B.F. Chau, G.K.M. Chan, Atomization of High-Viscosity Fluids for Aromatherapy Using Micro-heaters for Heterogeneous Bubble Nucleation, Sci. Rep. 7 (1) (2017) 1–14, https://doi.org/10.1038/srep40289.
[36] A. Lefebure, D. Shim, Ultrasonic atomization of highly viscous biodegradable oils for MQL applications, J. Mech. Sci. Technol. 35 (12) (2021) 5503–5516, https://doi.org/10.1007/s12206-021-1122-y.
[37] C. Li, C.Y. Lu, Y.X. Ma, S.Y. Li, W.Q. Huang, Design of an ultrasonic motor with multi-vibrators, J. Zhejiang Univ.-Sci. A 17 (9) (2016) 724–732, https://doi.org/10.1631/jzus.A1500316.
[38] Y. Liu, S. Shi, C. Li, W. Chen, J. Liu, A novel standing wave linear piezoelectric actuator using the longitudinal-bending coupling mode, Sens. Actuators, A 251 (2016) 119–125, https://doi.org/10.1016/j.sna.2016.10.015.
[39] S. Ueha, Ultrasonic motors theory and applications, Oxford Science Publications 7 (1993) 1–20.
[40] C.S. Zhao, Recent progress in ultrasonic motor techniques, J. Vib. Measur. Diagn. 24 (1) (2004) 1–5.
[41] D. Kang, K. Kim, D. Kim, J. Shim, D.G. Gweon, J. Jeong, Optimal design of high precision XY-scanner with nanometer-level resolution and millimeter-level working range, Mechatronics 19 (4) (2009) 562–570, https://doi.org/10.1016/j.mechatronics.2009.01.002.
[42] H. Yu, Y. Liu, X. Tian, S. Zhang, J. Liu, A precise rotary positioner driven by piezoelectric bimorphs: Design, analysis and experimental evaluation, Sens. Actuators, A 313 (2020), 112197, https://doi.org/10.1016/j.sna.2020.112197.
[43] J. Peng, L. Ma, X. Li, H. Tang, Y. Li, S. Chen, A novel synchronous micro motor for intravascular ultrasound imaging, IEEE Trans. Biomed. Eng. 66 (3) (2018) 802–809, https://doi.org/10.1109/TBME.2018.2856930.
[44] L. Wang, Y. Hou, K. Zhao, H. Shen, Z. Wang, C. Zhao, X. Lu, A novel piezoelectric inertial rotary motor for actuating micro underwater vehicles, Sens. Actuators, A 295 (2019) 428–438, https://doi.org/10.1016/j.sna.2019.06.014.
[45] W. Liang, J. Ma, C. Ng, Q. Ren, S. Huang, K.K. Tan, Optimal and intelligent motion control scheme for an Ultrasonic-Motor-Driven XY stage, Mechatronics 59 (2019) 127–139, https://doi.org/10.1016/j.mechatronics.2019.03.004.
[46] J. Stekke, C. Tendero, P. Tierce, C. Courtois, G. Rauwel, J. Lo, F. Pigache, Low-Voltage plasma Jet With piezoelectric generator: preliminary evaluation of decontamination capabilities, IEEE Trans. Plasma Sci. 48 (5) (2020) 1264–1270, https://doi.org/10.1109/TPS.2020.2985406.
[47] T. Sakayachi, Y. Nagira, M. Hikita, Study on achievement of simultaneous X, Y movements and theta rotation using straight-move ultrasonic vibrators. In: 2015 IEEE International Ultrasonics Symposium (IUS), 2015, pp. 1-4. https://doi.org/10.1109/ULTSYM.2015.0539.
[48] C.H. Sun, G.Q. Shang, Y.Y. Tao, Z.R. Li, A review on application of piezoelectric energy harvesting technology, Adv. Mat. Res. 516 (2012) 1481–1484, https://doi.org/10.4028/www.scientific.net/AMR.516-517.1481.
[49] G.Q. Shang, Y.Y. Tao, Z.R. Li, C.H. Sun, On piezoelectric harvesting technology, Adv. Mat. Res. 516 (2012) 1496–1499, https://doi.org/10.4028/www.scientific.net/AMR.516-517.1496.
[50] H.F. Zhang, B. Wang, A.L. Zhao, Research on power supply for adaptive ultrasonic vibration cutting based on piezoelectric technology, Agro Food Ind Hi Tech 28 (1) (2017) 2661–2665.
[51] M. Renaud, T. Sterken, A. Schmitz, P. A. F. P. Fiorini, C. A. V. H. C. Van Hoof, R. A. P. R. Puers, Piezoelectric harvesters and MEMS technology: fabrication, modeling and measurements. In: TRANSDUCERS 2007-2007 International Solid-State Sensors, Actuators and Microsystems Conference, 2007, pp: 891-894. https://doi.org/10.1109/SENSOR.2007.4300274.
[52] R. Ryndzionek, Ł. Sienkiewicz, A review of recent advances in the single-and multi-degree-of-freedom ultrasonic piezoelectric motors, Ultrasonics 116 (2021), 106471, https://doi.org/10.1016/j.ultras.2021.106471.
[53] X. Tian, Y. Liu, J. Deng, L. Wang, W. Chen, A review on piezoelectric ultrasonic motors for the past decade: Classification, operating principle, performance, and future work perspectives, Sens. Actuators, A 306 (2020), 111971, https://doi.org/10.1016/j.sna.2020.111971.
[54] N.W. Hagood, A.J. McFarland, Modeling of a piezoelectric rotary ultrasonic motor, IEEE Trans. Ultrason. Ferroelectr. Freq. Control 42 (2) (1995) 210–224, https://doi.org/10.1109/58.365235.
[55] Y. Ting, Y.R. Tsai, B.K. Hou, S.C. Lin, C.C. Lu, Stator design of a new type of spherical piezoelectric motor, IEEE Trans. Ultrason. Ferroelectr. Freq. Control 57 (10) (2010) 2334–2342, https://doi.org/10.1109/TUFFC.2010.1694.
[56] T. Lijima, M. Wada, Y. Nakagawa, H. Itoh, Ultrasonic motor using flexual standing wave, Japan. J. Appl. Phys. Suppl. 26 (S1) (1987) 191–193, https://doi.org/10.7567/JJAPS.26S1.191.
[57] J. Twiefel, W. Wurpts, J. Wallaschek, Theoretical and experimental treatment of standing wave type motors contact behavior. In: 2009 IEEE International Ultrasonics Symposium, 2009 pp: 1-4. https://doi.org/10.1109/ULTSYM.2009.5442023.
[58] K. Nakamura, M. Kurosawa, S. Ueha, Characteristics of a hybrid transducer-type ultrasonic motor, IEEE Trans. Ultrason. Ferroelectr. Freq. Control 38 (3) (1991) 188–193, https://doi.org/10.1109/58.79602.
[59] J.S.J. Satonobu, N.T.N. Torii, K.N.K. Nakamura, S.U.S. Ueha, Construction of megatorque hybrid transducer type ultrasonic motor, Jpn. J. Appl. Phys. 35 (9S) (1996) 5038, https://doi.org/10.1143/JJAP.35.5038.
[60] C. Zhao, Ultrasonic motors: technologies and applications, Springer Science & Business Media, 2011.
[61] T.L. Schmitz, K.S. Smith, Mechanical vibrations, Model. Measur. (2012).
[62] Z. Xu, Elastic mechanics, Higher Education, Beijing, 2006.
[63] W. Soedel, Vibrations of shells and plates, CRC Press, 2004.
[64] R.B. Bhat, Natural frequencies of rectangular plates using characteristic orthogonal polynomials in Rayleigh-Ritz method, J. Sound Vib. 102 (4) (1985) 493–499, https://doi.org/10.1016/S0022-460X(85)80109-7.
[65] A.W. Leissa, The free vibration of rectangular plates, J. Sound Vib. 31 (3) (1973) 257–293, https://doi.org/10.1016/S0022-460X(73)80371-2.
[66] J.Y. Zhang, Y.X. Du, J.Q. Liu, Y.R. Sun, Z.F. Yao, Q. Zhong, Experimental and numerical investigations of the collapse of a laser-induced cavitation bubble near a solid wall, J. Hydrodyn. (2022) 1–11, https://doi.org/10.1007/s42241-022-0017-4.
[67] E. Rood, mechanisms of cavitation inception, J. Fluids Eng. 113 (2) (1991) 163–175, https://doi.org/10.1115/1.2909476.